Aberrant visual population receptive fields in human albinism

Ethan J. Duwell

Department of Biophysics, Medical College of Wisconsin, Milwaukee, WI, USA ✉

Erica N. Woertz

Department of Cell Biology, Neurobiology, and Anatomy, Medical College of Wisconsin, Milwaukee, WI, USA ✉

Jedidiah Mathis

Department of Neurology, Medical College of Wisconsin, USA ✉

Joseph Carroll

Department of Biophysics, Medical College of Wisconsin, Milwaukee, WI, USA
Department of Cell Biology, Neurobiology, and Anatomy, Medical College of Wisconsin, Milwaukee, WI, USA
Department of Ophthalmology and Visual Sciences, Medical College of Wisconsin, Milwaukee, WI, USA ✉

Edgar A. DeYoe

Department of Radiology, Medical College of Wisconsin, Milwaukee, WI, USA ✉

Retinotopic organization is a fundamental feature of visual cortex thought to play a vital role in encoding spatial information. One important aspect of normal retinotopy is the representation of the right and left hemifields in contralateral visual cortex. However, in human albinism, many temporal retinal afferents decussate aberrantly at the optic chiasm resulting in partially superimposed representations of opposite hemifields in each hemisphere of visual cortex. Previous functional magnetic resonance imaging (fMRI) studies in human albinism suggest that the right and left hemifield representations are superimposed in a mirror-symmetric manner. This should produce imaging voxels which respond to two separate locations mirrored across the vertical meridian. However, it is not yet clear how retino-cortical miswiring in albinism manifests at the level of single voxel population receptive fields (pRFs). Here, we used pRF modeling to fit both single and dual pRF models to the visual responses of voxels in visual areas V1 to V3 of five subjects with albinism. We found that subjects with albinism (but not controls) have sizable clusters of voxels with unequivocal dual pRFs consistently corresponding to, but not fully coextensive with, regions of hemifield overlap. These dual pRFs were typically positioned at locations roughly mirrored across the vertical meridian and were uniquely clustered within a portion of the visual field for each subject.

Introduction

Retinotopic organization is one of the most fundamental and well-described organizational principles of visual cortex. Present at every level of the visual hierarchy, retinotopic organization is thought to play a vital role in the brain's ability to encode visual-spatial information. The establishment of retinotopic organization requires a surprising degree of connectional specificity during development. One promising route toward better understanding the development and functional organization of retinotopic maps is to study pathological syndromes where normal retinotopy is disrupted. In these cases, we can quantify exactly how retinotopic organization differs from normal and thereby provide a physiological basis for understanding and predicting potentially aberrant perceptual consequences.

Albinism is a well-known genetic syndrome characterized by disrupted melanin synthesis, which causes hypopigmentation of the eyes, and often the skin and hair. In addition, albinism is also associated with aberrant decussation of the temporal retinal afferents at the optic chiasm such that each cortical hemisphere receives substantial input from both the right and left visual hemifields of the same eye (Hoffmann, Tolhurst, Moore, & Morland, 2003;

Kaule, Wolynski, Gottlob, Stadler, Speck, Kanowski, Meltendorf, Behrens-Baumann, & Hoffmann, 2014; Morland, Baseler, Hoffmann, Sharpe, & Wandell, 2001). This results in overlaid retinotopic maps of significant portions of opposite hemifields within each hemisphere of occipital visual cortex. This differs from the arrangement in healthy, control subjects, where each hemisphere contains superimposed maps of the same (contralateral) hemifield from each eye (Horton & Hoyt, 1991). Thus, the pattern of miswiring in albinism represents a major disruption of normal retinotopic organization.

Previous functional magnetic resonance imaging (fMRI) mapping studies in albinism suggest that the right and left hemifield representations are superimposed in a precise manner such that each voxel responds to two regions at roughly mirror-image positions across the vertical meridian (VM) (Hoffmann et al., 2003). These results are generally consistent with the "true albino" pattern of hemifield superposition previously described in albino monkeys in which ocular dominance columns are supplanted by hemifield dominance columns (Guillery, Hickey, Kaas, Felleman, Debruyn, & Sparks, 1984; Hoffmann & Dumoulin, 2015). This columnar pattern was recently confirmed in high-resolution fMRI studies in human achiasma (Olman, Bao, Engel, Grant, Purington, Qiu, Schallmo, & Tjan, 2018) but has yet to be demonstrated in albinism. More recently, investigators have used single voxel population receptive field (pRF) modeling techniques to demonstrate the existence of single voxels with mirror symmetric, bilateral (dual) pRFs in achiasma and foveal hypoplasia, optic nerve decussation defects and anterior segment dysgenesis (FHONDA) syndrome (Ahmadi, Fracasso, van Dijk, Kruijt, van Genderen, Dumoulin, & Hoffmann, 2019; Hoffmann, Kaule, Levin, Masuda, Kumar, Gottlob, Horiguchi, Dougherty, Stadler, Wolynski, Speck, Kanowski, Liao, Wandell, & Dumoulin, 2012). These studies have assumed that subjects with albinism should present with the same mirror symmetric dual pRF topographies. However, this may not be the case as the genetic determinants and nature of retinocortical miswiring differ in achiasma, FHONDA, and albinism (Ahmadi et al., 2019; Hoffmann & Dumoulin, 2015). Recent reports also conflict regarding the existence of dual pRFs in albinism (Ahmadi, Herbik, Wagner, Kanowski, Thieme, & Hoffmann, 2019; Alvarez, Smittenaar, Handley, Liasis, Sereno, Schwarzkopf, & Clark, 2020; Carvalho, Invernizzi, Ahmadi, Hoffmann, Renken, & Cornelissen, 2020). A recent study by Alvarez et al. suggests that voxels in the overlap zone have discrete unilateral receptive fields while studies by Ahmadi et al. and Carvalho et al. support the existence dual receptive fields. Moreover, albinism itself is a heterogeneous syndrome with a wide variety of genetic and phenotypic subtypes (Montoliu, Grønskov, Wei, Martinez-Garcia,

Fernandez, Arveiler, Morice-Picard, Riazuddin, Suzuki, Ahmed, Rosenberg, & Li, 2014; Oetting, Summers, & King, 1994; Prieur & Rebsam, 2017; Simeonov, Wang, Wang, Sergeev, Dolinska, Bower, Fischer, Winer, Dubrovsky, Balog, Huizing, Hart, Zein, Gahl, Brooks, & Adams, 2013; Wilk, McAllister, Cooper, Dubis, Patitucci, Summerfelt, Anderson, Stepien, Costakos, Connor, Wirostko, Chiang, Dubra, Curcio, Brilliant, Summers, & Carroll, 2014). In a previous study (Woertz, Wilk, Duwell, Mathis, Carroll, & DeYoe, 2020), we described significant variation in the pattern of hemifield eccentricity mapping in subjects with albinism, thus suggesting that pRF properties in albinism may vary considerably across subjects.

In this study, we approached these issues using fMRI phase-encoded retinotopic mapping in combination with population receptive field modeling of voxels in V1 to V3 of subjects with genetically confirmed albinism. We tested the hypothesis that retinotopic mappings of opposite hemifield representations are partially superimposed in albinism and that individual voxels in these cortical regions of hemifield overlap have bilateral (dual) pRFs. Our results reveal imaging voxels with unequivocal dual pRFs in albinism consistently associated with the superimposed opposite hemifield representations. Although the two receptive field components of most dual pRFs were roughly symmetrical across the VM, others deviated significantly from precise symmetry. Dual pRFs also tended to cluster within discrete regions of the visual field, which were unique to each individual.

Methods

Subjects

The subject cohort and data used in this study are the same as in our recent study of cortical magnification in albinism (Woertz et al., 2020). Six subjects with albinism (4 women and 2 men; aged 15–31 years) with minimal nystagmus and five control subjects with no prior ocular or cortical pathology (2 women and 3 men; aged 20–25 years) were recruited for this experiment. One subject with albinism was excluded from further analysis due to significant motion artifacts in the fMRI data (boy, age 15 years). Genetic information and demographics for each albinism subject are listed in Table 1 below, and data characterizing fixation stability in each subject are presented in Table 2. Retinal features and cortical magnification in these subjects are described in detail elsewhere as are the methods used to determine best corrected visual acuity (BCVA), albinism subtype, and genetic mutations (Wilk et al., 2014; Wilk, Wilk, Langlo, Cooper, & Carroll, 2017; Woertz et al., 2020). It is also notable that subjects 2 and 4 are siblings with

Subject	ID[*]	Age (year)	Sex	BCVA	Albinism subtype	Mutations
1	JC_10227	19	F	20/40 (OU)	OCA2	*OCA2* c.1327G>A; p.V443I *TYR* c.575C>A; p.S192Y
2[†]	JC_0492	31	F	20/25 (OU)	OCA1	*TYR* c.1147G>A; p.D383N *TYR* c.1217C>T; p.P406L
3	JC_10230	18	F	20/50 -2 (OU)	OCA1	*TYR* c.575C>A; p.S192Y (hom) *TYR* c.1205G>A; p.R402Q *TYR* c.1265G>A; p.R422Q
4[†]	JC_0493	23	F	20/20- (OU)	OCA1	*TYR* c.1147G>A; p.D383N *TYR* c.1217C>T; p.P406L
5	JC_10093	19	M	20/100 +2 (OD) 20/80 +2 (OS)	OA	*GPR143* c.346T>G; p.C116G *TYR* c.1205G>A; p.R402Q (hom)
6[‡]	JC_10278	19	M	20/32 (OU)	OCA1	*TYR* c.286_287insA; fs *TYR* c.575C>A; p.S192Y*TYR* c.1205G>A; p.R402Q

Table 1. Genetics and demographics for subjects with albinism.
*ID used in Wilk et al. (2014) and Wilk et al. (2017).
†Subjects are sisters.
‡Excluded due to motion artifact.
(hom) = homozygous; OCA = oculocutaneous albinism; OA = ocular albinism (X-linked).

		OD		OS	
Subject	ID	50% BCEA	95% BCEA	50% BCEA	95% BCEA
1	JC_10227	0.24	1.05	0.45	1.95
2	JC_0492	0.04	0.19	0.06	0.28
3	JC_10230	1.92	8.35	0.62	2.68
4	JC_0493	0.84	3.66	0.14	0.597
5	JC_10093	3.68	16.01	5.97	25.95

Table 2. Fixational stability in subjects with albinism. OD = right eye; OS = left eye; BCEA = bivariate contour ellipse area. All values are expressed in degrees^2.

identical mutations. Finally, subject 1 had only one OCA2-related mutation; however, we classified this subject as having OCA2 as she had no known mutations in any other albinism-causing genes. The study was in accordance with the Declaration of Helsinki and approved by the Institutional Review Board of the Medical College of Wisconsin. All subjects provided written informed consent after explanation of the nature and possible risks and benefits of the study.

Fixation testing

An in-depth description of the fixation testing method performed on these subjects is described elsewhere (Woertz et al., 2020). In brief, subjects fixated on a small white cross while their fixation stability was monitored using the fixation test module of an OPKO combined scanning laser ophthalmoscope (SLO). These retinal imaging data were then used to compute the 50% and 95% bivariate contour ellipse areas (BCEA) that characterize each subject's fixation stability.

fMRI visual stimuli

Please note that the following descriptions of the fMRI visual stimuli, fMRI stimulus paradigm, fMRI acquisition, phase encoded retinotopic maps, and visual area mapping are nearly identical to those described in our recent study of cortical magnification in albinism (Woertz et al., 2020). This study utilizes the same fMRI data.

All visual stimuli for fMRI were presented on a back-projection screen mounted on the MRI head coil. A BrainLogics BLMRDP-A05 MR digital projector was used with a ViSaGe MKII visual stimulus generator (Cambridge Research Instruments) in conjunction with custom MATLAB software. Stimuli subtending a maximum of 20 degrees eccentricity included conventional expanding ring and rotating wedge retinotopic mapping stimuli (DeYoe, Carman, Bandettini, Glickman, Wieser, Cox, Miller, & Neitz, 1996). Rings and wedges were composed of black and white counterphase flickering (8 Hz) circular checkerboards with check size and ring width scaled with eccentricity. Stimuli were photopic and presented on a uniform gray background. All subjects were instructed to continually fixate on a marker at the center of the screen. To enhance stable fixation, thin, black radial lines extending from fixation to the edge of the display were present continuously during all tasks.

To avoid collecting redundant MRI data on control subjects, we used previously acquired retinotopic mapping data even though it was obtained with a slightly different experimental protocol than for subjects with albinism. However, due to the temporal phase mapping methods used in this study, retinotopic parameters (eccentricity and polar angle) that are

encoded by the timing of the fMRI responses did not appear to be significantly affected by the stimulus differences. For subjects with albinism, the wedge stimuli subtended 45 degrees polar angle, whereas for control subjects the wedges subtended 90 degrees. All subjects viewed both ring and wedge stimuli binocularly with full-field stimulation. Additionally, for subjects with albinism, the expanding ring stimuli were presented to the right and left hemifields in separate runs and were tested separately for each eye. The hemifield ring stimuli were identical to the full field version, except that one hemifield was masked to match the grey background. For control subjects, the ring stimulus expanded from the center to the periphery in 40 seconds and was repeated five times per run. For subjects with albinism, both the full-field and hemifield ring stimuli expanded from 0.8 degrees eccentricity to the periphery in 60 seconds and were repeated five times per run. For subjects with albinism, the center of the display consisted of a circular black and white disc (similar to a radioactivity symbol) with a radius of 0.8 degrees that flickered at random intervals not synchronized to the rings or wedges presentation. To control attention, subjects were instructed to press and hold a button whenever the central disc flickered.

fMRI stimulus paradigm

Control subjects completed all imaging during a single session. Subjects with albinism completed imaging during two sessions: the right eye hemifield expanding ring tasks in the first session, and all remaining tasks in the second session. All monocular hemifield runs were repeated five times and binocular full-field runs were repeated three times. For monocular stimuli, repetitions of the right and left hemifield stimuli were interleaved; for full-field stimuli, repetitions of the expanding ring and rotating wedge were interleaved. After each fMRI run, the subject was asked to rate their alertness on a scale from 1 to 5 (1 being asleep and 5 being fully awake). This measure was used to control for subjects' alertness, which can affect the quality of data. We used this measure as an exclusion criterion. However, no subjects were excluded from this study for poor alertness.

fMRI acquisition

MRI scans were obtained at the Medical College of Wisconsin using a 3.0 Tesla General Electric Signa Discovery 750 MRI system equipped with a custom 32-channel RF/gradient head coil. BOLD fMRI images were acquired with a T2*-weighted gradient-echo EPI pulse sequence (TE = 25 ms, TR = 2 seconds, and FA = 77 degrees). The 96 × 96 acquisition matrix (Fourier interpolated to 128 × 128) had frequency encoding in the right-left axial plane, phase encoding in anterior-posterior direction and slice selection in the axial direction. The FOV was 240 mm and included 29 axial slices covering the occipital lobe and adjacent portions of the temporal and parietal lobes with a slice thickness of 2.5 mm, yielding a raw voxel size of 1.875 × 1.875 × 2.5 mm. For anatomic scans, a T1-weighted, spoiled gradient recalled at steady state (SPGR), echo-planar pulse sequence was used (TE = 3.2 ms, TR = 8.2 ms, and FA = 12 degrees) with a 256 × 224 acquisition matrix (Fourier interpolated to 256 × 256). The FOV was 240 mm, and 180 slices with a slice thickness of 1.0 mm, yielding voxel sizes of 0.938 × 0.938 × 1.0 mm^3. The SPGR scans were subsequently resampled to 1.0 mm^3. A sync pulse from the scanner at the beginning of each run triggered the onset of visual stimuli.

Analysis software

All fMRI data were analyzed using the AFNI/SUMA software package (version: AFNI_19.1.11, https://afni.nimh.nih.gov/) (Cox, 1996). Surface models were produced from the high resolution SPGR images using the "recon-all" function in Freesurfer (version 5.1.0 and 5.3.0, http://surfer.nmr.mgh.harvard.edu/). Single voxel time-course modeling was performed using custom software in MATLAB (R2017b).

fMRI pre-processing

The fMRI pre-processing was performed using a script generated by AFNI's afni_proc.py command, and occurred in the following order: reconstruction, removal of before and after periods, slice timing correction, alignment and volume registration, smoothing, scaling, regression of motion parameters and linear trends, and averaging. Before and after periods were removed using AFNI 3dTcat, and slice time shift correction was then performed using AFNI 3dTshift. To reduce alignment bias for scans acquired during either of the two imaging sessions in our albinism subjects, the reference SPGR anatomic images from both sessions were skull-stripped using AFNI 3dSkullStrip, aligned using AFNI align_epi_anat.py, and averaged using AFNI 3dMean to create an average reference anatomy for the two sessions. For control subjects, all data were acquired in a single session, so the creation of an average reference anatomy was not necessary. The alignment of functional runs for control subjects was otherwise identical to subjects with albinism. Rigid body alignment and volume registration were performed using AFNIs align_epi_anat.py and 3dVolreg, respectively. During volume registration, volumes in each run were

registered to the volume in that series having the least motion as computed by AFNI 3dToutcount. This volume was also used as the base EPI for aligning each functional run to the anatomic scan. The alignment and volume registration transformations were computed separately, concatenated, and then applied together. Registration parameters from 3dVolreg were used to compute motion magnitude time series to serve as motion regressors later in the pipeline. Each run was then smoothed with a 3.75 mm (full width at half maximum) Gaussian kernel using AFNI 3dMerge, and then brain-masked using 3dAutomask. After masking, the timeseries data were then scaled to range from 0 to 200 with a mean of 100. Linear trends were then removed from the scaled data and a regression analysis of the motion regressors was then performed using 3dDeconvolve. The resulting motion regression matrix was projected out of the time series data using 3dTproject. Finally, individual runs from each task were averaged using 3dMean.

Phase encoded retinotopic maps

The spatial distributions of significant fMRI responses for each functional task were displayed as phase encoded retinotopic activation maps. Significant responses were identified by cross correlating the empirical time course data for each voxel with a reference waveform using AFNI 3ddelay (Bandettini, Jesmanowicz, Wong, & Hyde, 1993; Datta & DeYoe, 2009; Saad, DeYoe, & Ropella, 2003). This analysis produces the correlation coefficient and phase values at the phase offset of maximum correlation for each voxel. The reference waveform used for this phase mapping procedure was a binary square wave describing the stimulus cycles convolved temporally with the "Cox Wide" estimation of the hemodynamic response function (HRF).

Visual area mapping

The correlation analysis described above was performed on the smoothed, full field, phase encoded retinotopy data, and the results were projected onto cortical surface models in AFNI/SUMA. These phase encoded polar angle and eccentricity maps were used to identify and map visual areas V1 to V3 in both albinism subjects and controls using criteria previously reported by a number of laboratories (Amano, Wandell, & Dumoulin, 2009; Arcaro, McMains, Singer, & Kastner, 2009; DeYoe et al., 1996; Engel, Glover, & Wandell, 1997; Hansen, Kay, & Gallant, 2007; Pitzalis, Galletti, Huang, Patria, Committeri, Galati, Fattori, & Sereno, 2006; Pitzalis, Sereno, Committeri, Fattori, Galati, Patria, & Galletti, 2010; Sereno, Dale, Reppas,

Kwong, Belliveau, Brady, Rosen, & Tootell, 1995; Sereno, Pitzalis, & Martinez, 2001; Silver & Kastner, 2009; Swisher, Halko, Merabet, McMains, & Somers, 2007; Wandell, Dumoulin, & Brewer, 2007; Wandell & Winawer, 2011). Visual area regions of interest (ROIs) drawn on the cortical surface models were then transformed back to the volumetric domain using AFNI's 3dSurf2Vol.

Identifying cortical zones of right-left hemifield overlap in albinism

To identify cortical regions responding to both the right and left hemifields for each individual subject with albinism, the monocular right and left hemifield eccentricity maps from both eyes were thresholded to a minimum correlation coefficient of 0.45, binarized, and then logically combined using AFNI's 3dcalc to generate hemifield overlap maps. Our choice of threshold was intentionally conservative relative to other studies so as to avoid potentially equivocal overlap regions (Alvarez et al., 2020; Hoffmann et al., 2003; Kaule et al., 2014; Woertz et al., 2020). Any voxel which responded above threshold in both a left and right hemifield stimulation condition was included in the hemifield overlap ROI. Voxels which responded to only a single hemifield were included in the non-overlap ROI.

Population receptive field modeling

Both single and dual Gaussian pRF models were optimized for each responsive voxel to fit the full field rotating wedge time-course data in visual areas V1 to V3. The procedure was inspired by methods developed by Dumoulin et al. (Dumoulin & Wandell, 2008) but was implemented independently using custom Matlab software (Puckett & DeYoe, 2015). The modeling algorithm uses properties of the stimuli, tasks, and BOLD hemodynamics in conjunction with estimates of the pRF to generate a predicted fMRI waveform. This predicted waveform was then fit to the empirical time-course data yielding an error signal, which was used to drive an iterative optimization of the Gaussian model parameters so as to fit the empirical data most accurately. Single pRFs were modeled as a simple 2D Gaussian:

$$g(x, y) = Ae^{-\frac{(x-x_0)^2+(y-y_0)^2}{2\sigma_1^2}} \quad (1)$$

where (x_0 and y_0) is the center position, σ is the standard deviation of the distribution, and A is an

amplitude scaling factor. Dual pRFs were modeled as the sum of two independent 2D Gaussians:

$$g(a, b, x, y) = A_1 e^{-\frac{(a-a_0)^2+(b-b_0)^2}{2\sigma_1^2}} + A_2 e^{-\frac{(x-x_0)^2+(y-y_0)^2}{2\sigma_2^2}} \quad (2)$$

where (a_0 and b_0) and (x_0 and y_0) are the centers of the two Gaussians, σ_1 and σ_2 are the standard deviations of the two Gaussians, and A_1 and A_2 are the amplitude scaling factors.

The modeling procedure began by multiplying an initial pRF estimate with the spatial pattern of the stimulus and integrating over space at each time point to generate an ideal "neural" response waveform. This ideal response was then convolved temporally with an estimate of the HRF to produce a predicted fMRI response. The residual sum squared error (RSS) between this predicted response and the empirical fMRI waveform was then computed. The RSS error signal drove an iterative optimization of the location, standard deviation, and amplitude parameters of the model searching for the combination which produced a minimum error in the fit between the model's predicted time course and the voxel's empirical time course. Optimization began with a coarse grid search of all possible (a_0 and b_0) and (x_0 and y_0) starting positions limited to the voxel's preferred eccentricity as determined by the full field expanding ring experiment. Using the starting positions established by the coarse search, polar angle, σ, and amplitude (sensitivity) were refined in a two-pass, coarse-to-fine fashion using an unconstrained nonlinear optimization algorithm (Matlab's fminsearch) to obtain an optimal fit to the empirical rotating wedge fMRI waveform.

This process was performed twice for each voxel: once with the single Gaussian pRF model, and again with the dual Gaussian model. We emphasize that for the dual Gaussian model, each Gaussian was optimized independently. Previous papers performing dual receptive field modeling in albinism, achiasma, and other misrouting disorders have restricted the two receptive fields to be at mirror image locations either across the VM, horizontal meridian (HM), or fixation (Ahmadi et al., 2019; Ahmadi et al., 2019; Alvarez et al., 2020; Hoffmann et al., 2012). By allowing the two Gaussians to be optimized independently, our model tested the possibility that dual pRFs in albinism may be arranged at any combination of angular positions at a given eccentricity.

Voxel selection

All of our quantitative analyses were performed only on voxels falling within our V1 to V3 visual area ROIs. Selection criteria varied slightly in each separate analysis. To be included in our hemifield overlap analysis, voxel responses were required to achieve a correlation coefficient greater than 0.45 on at least one of the four monocular hemifield stimulation conditions. For voxels to be included in our pRF analysis, one of the two pRF models must have explained a minimum of 20% of the total time course variance for that voxel. The percent variance explained by each model was calculated using Equation 4 below. For inclusion in our analysis of the incidence of dual pRF voxels in hemifield overlap versus nonoverlap zones in albinism, voxels were required to meet both of the criteria above. In addition, as wedge and ring stimuli for the albinism group did not overlap the central 0.8 degrees of visual space (obscured by central fixation task stimulus), we excluded voxels responding to the central most 1 degree of visual space in both the albinism and control groups. This also served to eliminate artifacts known to occur at the center of gaze when using ring and wedge stimuli.

Model comparisons

The fits of the single and dual pRF models for each voxel were compared using a partial *F*-test to determine whether the additional Gaussian parameters optimized in the dual pRF model resulted in a significant increase in variance explained. For each voxel, a partial *F*-static was computed using the following equation:

$$F = \left(\frac{\frac{RSS_S - RSS_D}{df_S - df_D}}{\frac{RSS_D}{df_D}} \right) \quad (3)$$

Where RSS_S is the *RSS* error from fitting the single pRF model, RSS_D is the *RSS* error from fitting the dual pRF model, df_S is the number of degrees of freedom in the single pRF model, and df_D is the number of degrees of freedom in the dual pRF model. Df_S and df_D included the number of free parameters optimized in the single and dual pRF models respectively plus the number of degrees of freedom used in the baseline motion/linear trends regression model projected out of the time series data during pre-processing. Voxels were considered to have dual pRFs if this partial *F*-statistic fell above the 99% confidence interval in the appropriate *F*-distribution. Voxels were considered to have single pRFs if their *F*-statistic fell below the 1% confidence interval. (In other words, only voxels from either extreme of the distribution were selected, thereby excluding voxels with ambiguous signals.) Our selection criteria were intentionally conservative and were intended to select the most unequivocal dual and single pRF voxels for use in subsequent analyses. We note that the *F*-test assumes that all measurements are fully independent, which is not necessarily true for

adjacent fMRI time points (Raz, Zheng, Ombao, & Turetsky, 2003). However, we also assess the model fits in these same voxels using cross-validation (described below), which does not rely on this assumption. The percent variance explained (%*VE*) by each respective model was also computed on a voxel-wise basis using the following equation:

$$\%VE = 100 \times \left(\frac{TSS - RSS}{TSS} \right) \quad (4)$$

Where *TSS* is the total sum of squares for the voxel time course and *RSS* is the RSS error from the model fitting. Finally, the difference in variance explained (ΔVE) by the dual and single pRF models was computed for each voxel in the following manner:

$$\Delta VE = \%VE_{dual} - \%VE_{single} \quad (5)$$

Where $\%VE_{dual}$ and $\%VE_{single}$ are the percent variance explained by the dual and single pRF models, respectively.

To further assess whether the additional variance explained by the dual pRF model was caused by over-fitting due to the extra model parameters, we also performed a cross-validation analysis. All voxels in the albinism group meeting the single or dual pRF criteria described above were included in this analysis. The cross-validation had two stages: a training stage and a validation stage. During the training stage, we split each subject's rotating wedge data into the three individual runs and fit both the single and dual pRF models to each run. The mean %*VE* for each model was computed for each run in each subject. These were then averaged across subjects to compute the mean %*VE* for each model during training. During the validation stage, we tested the models trained on each individual run by separately computing %*VE* in each of the other two runs. The mean %*VE* for each model was computed for all six train-test combinations (using the 3 runs) in each subject. These were then averaged across subjects to compute mean %*VE* for the single and dual pRF models during validation. If the additional parameters in the dual model were simply over-fitting noise in the training data, they should provide no benefit over the single pRF model in the validation stage. However, if the dual pRF model explains significantly more stimulus-driven variance than the single model, it should do so in both stages.

Dual pRF symmetry

For all dual pRF voxels, the degree to which the dual pRFs were symmetric across the VM was assessed by computing the angle (θ) between the two pRF centers with respect to the HM:

$$\theta = Tan^{-1} \left(\frac{y_2 - y_1}{x_2 - x_1} \right) \quad (6)$$

Where (x_1 and y_1) are the Cartesian coordinates for pRF center 1 and (x_2 and y_2) are the coordinates for pRF center two. The absolute values of these angles can range from 0 degrees to 90 degrees. Because the dual pRF components were constrained to be at the same eccentricity, an angle of 0 degrees indicated symmetry across the VM, and 90 degrees indicated symmetry across the HM. Histograms of dual pRF angles were generated for each subject.

Results

Fixational stability

A detailed discussion of the fixation stability results in these subjects is provided in our recent paper on cortical magnification in albinism (Woertz et al., 2020). The 50% and 95% BCEA for each eye in each subject with albinism are shown in Table 2. All but one subject's (subject 5) 50% BCEAs were below 3.14 deg², the threshold previously used to define normal steady fixation (Fujii, De Juan, Humayun, Sunness, Chang, & Rossi, 2003; Woertz et al., 2020).

Aberrant retinotopic organization in albinism

As reported in the previous literature (Hoffmann et al., 2003; Kaule et al., 2014; Morland et al., 2001; Prieur & Rebsam, 2017), we observed overlapping representations of both left and right hemifields within each cerebral hemisphere of all our subjects with albinism. Figures 1A and 1B display inflated cortical surface maps of the left occipital lobe in one representative subject with albinism (subject 5). In this case, right (A) and left (B) hemifield expanding ring stimuli were presented monocularly to the right eye. The eccentricity color code is shown in the upper left of Figures 1A and 1B. By visual inspection, the right and left hemifield eccentricity maps appeared to be grossly in register but the aberrant left hemifield representation (B) was less complete than the normal right hemifield representation (A) such that the two maps only partially overlap. The foveal representation in this subject, which should be at the occipital pole, was reduced relative to our control subjects, consistent with previous observations (Woertz et al., 2020). Monocular right and left hemifield eccentricity maps from each eye
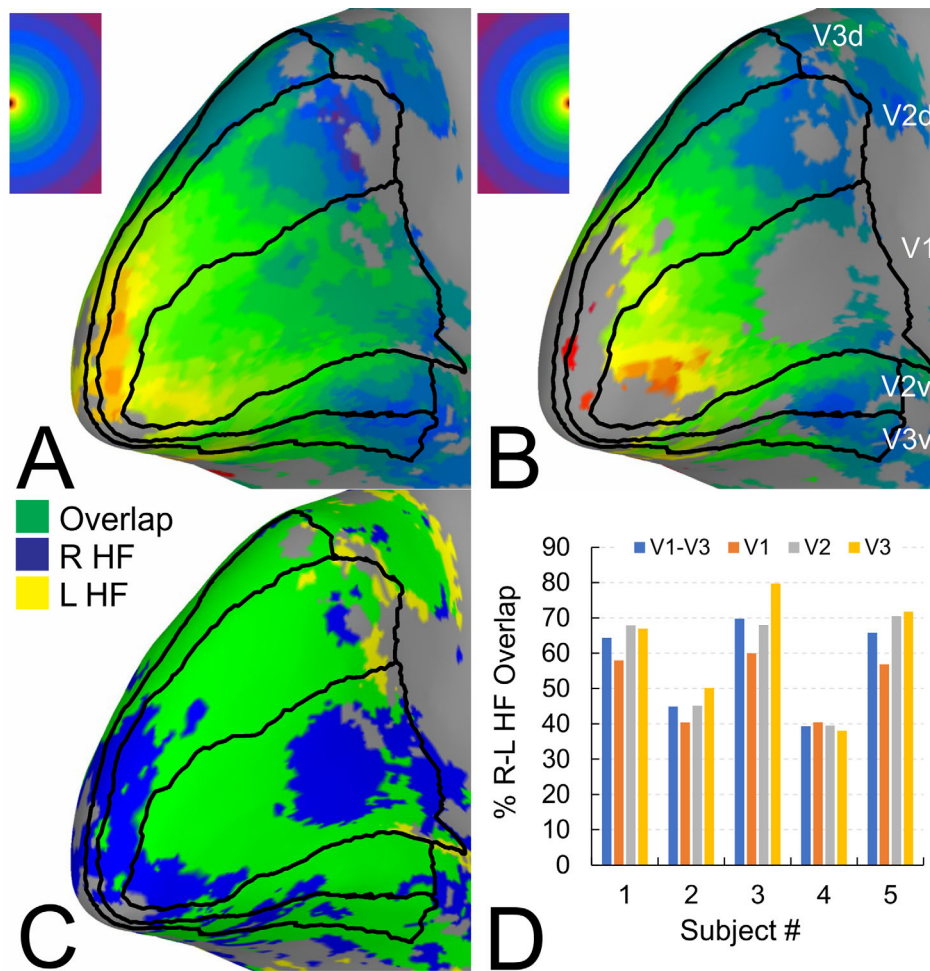
Figure 1. Monocular (right eye) hemifield eccentricity maps and overlap. (**A**) Right hemifield stimulus condition. (**B**) Left hemifield stimulus condition. (**C**) Hemifield overlap map. Green is the logical intersection of A and B after thresholding. (D) Percent hemifield overlap in V1 to V3. Data combined across all eye-hemifield stimulus conditions. Color codes for eccentricity and overlap maps are in upper left corner of **A–C**. Thin black lines demarcate V1 to V3 visual area boundaries. All maps are displayed on left occipital cortex surface model for a representative subject with albinism.

are illustrated for both hemispheres for each subject with albinism in Supplementary Figure S1.

The right and left hemifield representations in Figures 1A and 1B were combined logically in Figure 1C to form a right-left hemifield overlap map. In this map, the blue regions responded exclusively to the right hemifield, yellow regions responded exclusively to the left hemifield, and the green "overlap" regions responded to both hemifields. As displayed in Figure 1C, irregular swaths of hemifield overlap (green) are interspersed with right hemifield patches (blue) both ventrally and dorsally in V1, V2, and V3 (black outlines). The extent of hemifield overlap is quantified in Figure 1D for V1 to V3 in each of our five subjects with albinism. Here, data were combined across all stimuli, eye conditions, and hemispheres. To be classified as "overlapping," a voxel was required to respond above threshold ($cc > 0.45$) to both a right and

left hemifield stimulus regardless of the eye stimulated. Within individual subjects, the percent overlap tended to be similar across V1 to V3. However, there were considerable differences in the mean percent overlap across subjects with values ranging from 39% to 70%.

Line of decussation shift

To quantify the degree to which the line of decussation shifted in each subject, we estimated the maximum horizontal extent of the aberrant ipsilateral hemifield representations. Using the approach described in Hoffmann et al. (2003), we drew ROIs for each subject encompassing the HM representation along the fundus of the calcarine sulcus in V1. We then made eccentricity histograms for responsive voxels within these ROIs for each of our monocular hemifield

Subject #	Max horizontal ipsilateral field eccentricity (degrees)		Max horizontal contralateral field eccentricity (degrees)	
	Left hemisphere right eye left hemifield	Right hemisphere left eye right hemifield	Left hemisphere right eye right hemifield	Right hemisphere left eye left hemifield
1	9.7	13.8	14.0	13.5
2	4.3	3.0	13.3	14.7
3	6.7	7.9	13.4	13.6
4	6.1	3.9	14.1	13.5
5	9.4	8.8	12.5	13.4

Table 3. Estimation of aberrant decussation extent in albinism.

stimulation conditions. The maximum eccentricity that encompassed 95% of the data points in the aberrant representation was then used as the measure of decussation shift. To avoid artifactual outliers common at high eccentricities, we limited this analysis to voxels with eccentricity values from 1 to 15 degrees. These data are listed below in Table 3. As the primary aberrant decussation in albinism consists of temporal retinal afferents from each eye decussating to the contralateral hemisphere, we have only listed data in each hemisphere from the contralateral eye stimulation condition. Data for the aberrant ipsilateral field representations in each hemisphere are listed on the left, and the data for the normal contralateral field representations are listed on the right. Aberrant ipsilateral field representations extended horizontally between 3.0 and 13.8 degrees. This is comparable to previous in reports by Hoffmann et al. in which the aberrant representations extended 5.5 to 13.9 degrees (Hoffmann et al., 2003). By comparison, the normal contralateral representations extended between 12.5 and 14.7 degrees. Because we computed the 95% threshold as our measure of maximum horizontal eccentricity, these values do not quite extend to 15 degrees in the normal representations. We were not able to compute this metric in our controls as they did not undergo the hemifield stimulation paradigm; however, Hoffmann et al. estimated that ipsilateral field representations in controls extend horizontally between 0 and 4.1 degrees eccentricity (Hoffmann et al., 2003). The extent of ipsilateral activation in controls was also reported in (Tootell, Mendola, Hadjikhani, Liu, & Dale, 1998).

pRFs in albinism

The partial overlap of opposite hemifield representations in visual cortex gives rise to voxels with either single or dual responses to the rotating wedge stimulus. As illustrated in Figure 2A (left), the unusual dual responses (green traces) were easily identified in the rotating wedge time course data because they showed 10 robust peaks even though the wedge rotation had only five cycles. Yet, other voxels within the same individual responded to the same stimulus with the more typical five peaks (see Figure 2A right). These results are consistent with some voxels responding to two visual field loci per cycle, whereas other voxels respond to a single locus per cycle. To test this quantitatively, we fit each voxel's time course with both a single Gaussian and a dual Gaussian pRF model. In the top row of Figure 2A, we display the time course predicted by the dual pRF model (black trace) and in the bottom row we display the single pRF prediction. For the voxel illustrated in the left panel of Figure 2A, the dual Gaussian pRF model is able to fit all 10 response peaks whereas the single Gaussian model only fits half the peaks. As a result, there is a substantial difference in variance explained ($\Delta VE = 32.42\%$) by the two models (77.25% vs. 39.83%, $F = 11.4$, $p < 0.001$). However, for the voxel time course shown in the right panels, there are only five peaks to fit. Consequently, the additional Gaussian parameters of the dual model provide less benefit, and there is little difference in variance explained ($\Delta VE = 0.06\%$) by the two models (70.04% vs. 69.97%, $F = 0.02$, $p > 0.999$). (Note: Because the two pRF components are fit independently, they tend to be forced into the same visual field locations when the empirical waveform has only five peaks, thus the two models tend to explain the same amount of variance.)

Figure 2B shows the voxel-wise difference in variance explained by the two models as a colored pattern across the cortical surface for subject 5. There are clearly large clusters of voxels (yellow patches) in which the dual pRF model explains substantially more variance than the single pRF model, sometimes as much as an additional 40% of the total time course variance for the voxel.

Figure 2C displays the results of the partial F-test from the comparison of the two models (see Methods) for the same subject. In this analysis, "dual pRF voxels" (red) must have an F-value above the 99% confidence interval, and single pRF voxels (purple) must have an F-value below the 1% confidence interval. It is notable that dual pRF voxels occurred in large contiguous clusters often, although not always, near the HM representations in V1 and on the V2 to V3 boundary,
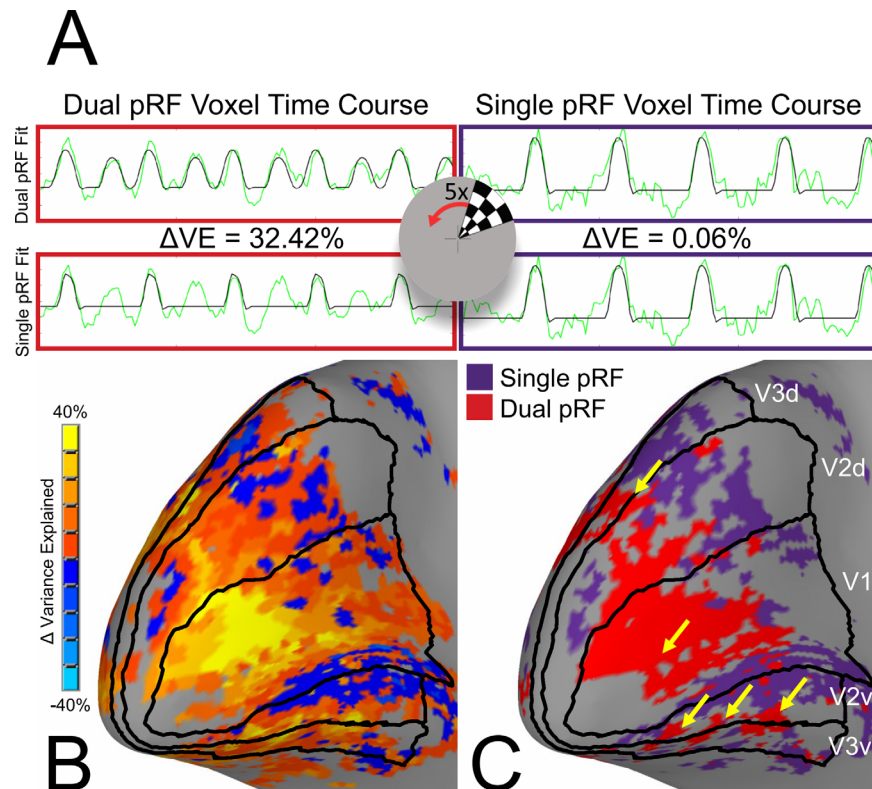
Figure 2. Time courses and distribution of single versus dual pRF voxels for one subject with albinism. (**A**) Representative fMRI time courses (green) for one voxel classified as having a dual pRF (left, red outline) and one voxel classified as having a single pRF (right, purple outline). Black traces represent the dual (top) versus single (bottom) pRF model predictions and $\triangle VE$ is the difference in variance explained by the two models ($\triangle VE = \%VE_{dual} - \%VE_{single}$). Center overlay depicts a single frame of the rotating wedge stimulus. (**B**) Brain map of $\triangle VE$ with color code at left. (**C**) Distribution of single (purple) versus dual (red) pRF voxels. Arrows point to dual pRF clusters observed to repeat along HM representations.

as indicated by the yellow arrows in Figure 2C. In contrast, the single pRF voxels tended to cluster near the VM representations.

Incidence and cortical distribution of single and dual pRF voxels

Voxels meeting the dual pRF criteria were observed in V1, V2, and V3. Figure 3A displays examples of the rotating wedge time courses from several dual pRF voxels in V1 to V3 of a representative subject with albinism. Again, the green traces are the empirical rotating wedge time courses, and the black traces are the model predications. The corresponding dual pRF models are represented in visual space in the right column. Note that these voxels all responded to dual locations in opposite hemifields that were approximately mirrored across the VM. The mean incidence of dual pRF voxels for both albinism and control groups is summarized in Figure 3B for V1, V2, and V3 separately as well as combined. Percent dual pRF incidence was compared across groups and

visual areas using a 2-way ANOVA. This test showed a significant group effect ($p < 0.001$) but no significant visual area effect ($p = 0.592$) or interaction. Post hoc tests showed that subjects with albinism had higher incidences of dual pRF voxels than controls in every visual area (2-tailed, independent t-tests, p values for V1, V2, and V3, respectively: $p = 0.006$, $p = 0.006$, and $p = 0.013$). On average, dual pRF voxels comprised 8.6% of all visually responsive voxels in the albinism group but ranged from 4% to 15% for different subjects with albinism. This underscores the fact that dual pRF voxel incidence varies across subjects. In contrast, the mean incidence of dual pRFs in control subjects was 1.8% with individual values ranging from of 1% to 3%. Furthermore, visual inspection of many "dual pRF" voxels in controls revealed that they tend to be voxels sampling across the midline or cases in which clear five peaked fMRI responses were overfit by the dual model.

Cross-validation

To further test whether the additional variance explained by the dual pRF model is due to over-fitting
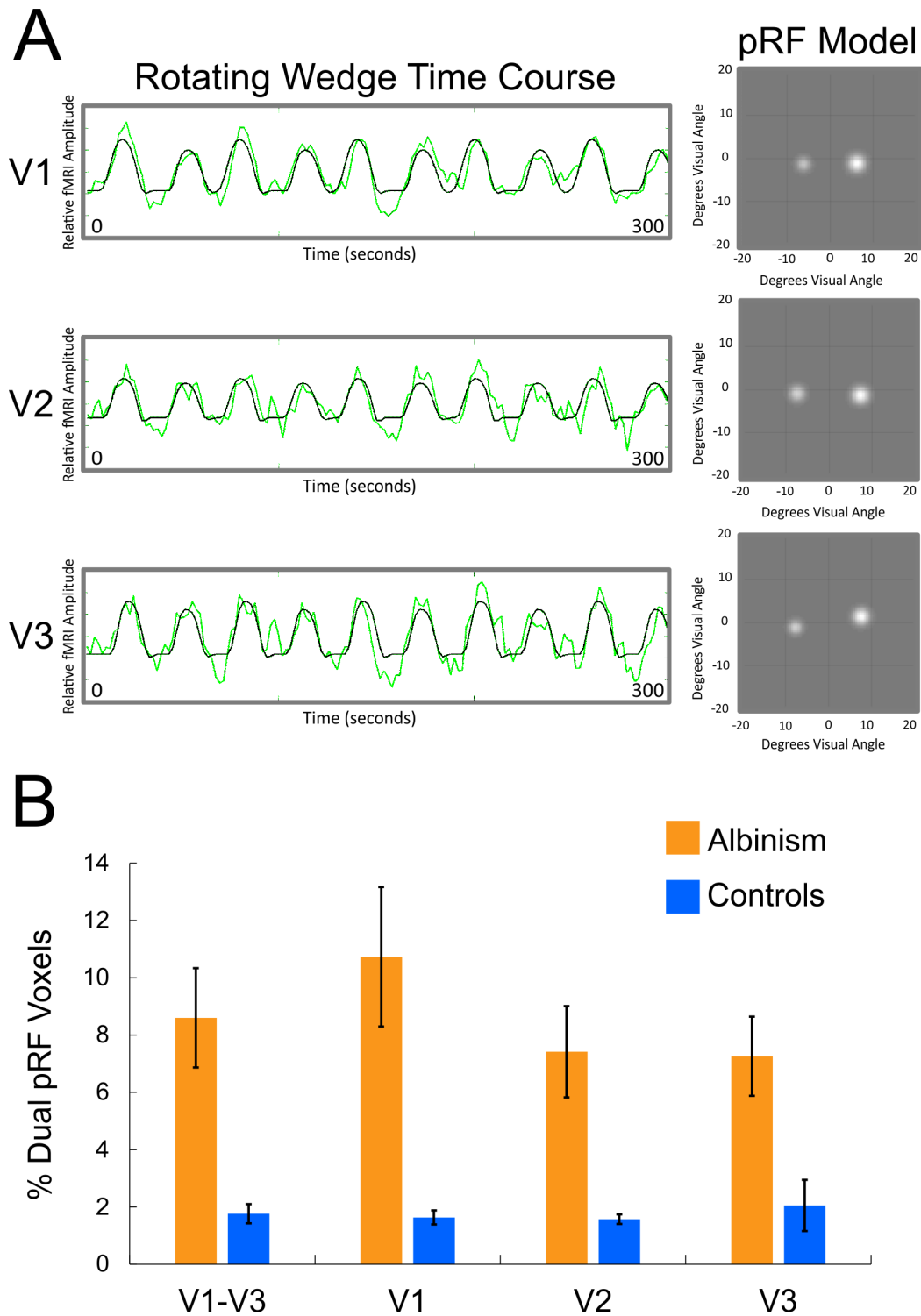
Figure 3. (**A**) The fMRI time courses (green) and dual pRF model predictions (black) for representative voxels with dual pRFs in V1 to V3 of one subject with albinism. Right: Dual pRF models in visual space. White spots represent Gaussian sensitivity profiles for each dual pRF component. (**B**) Percent incidence of dual pRF voxels in V1 to V3 for the albinism and control groups. Subjects with albinism had significantly greater dual pRF incidence in V1, V2, and V3 individually as well as combined across visual areas (respective *p* values: 0.006, 0.006, 0.013, and 0.005). Error bars are *SEM*.
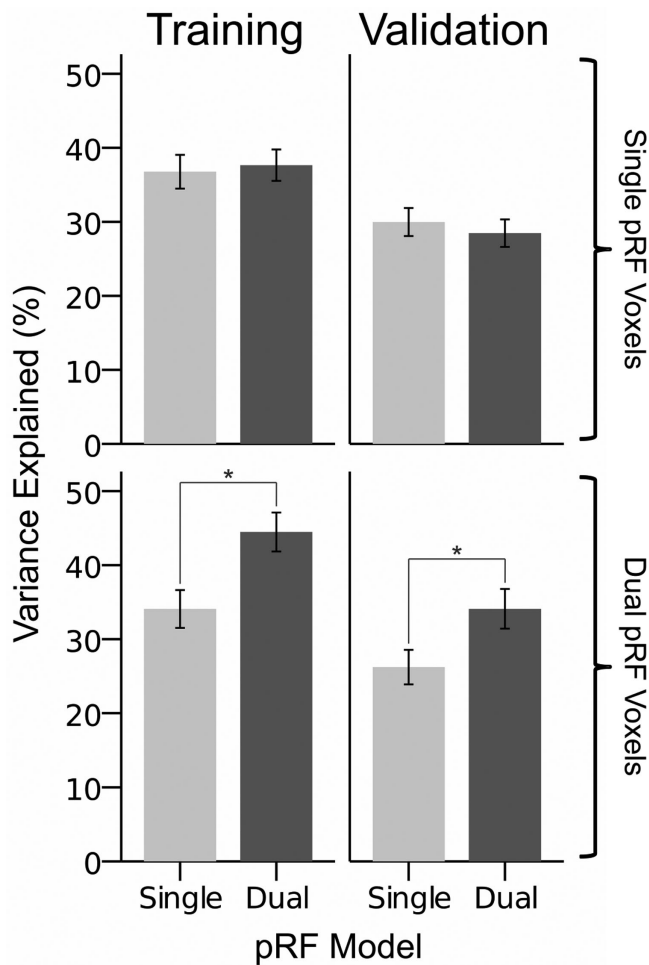
Figure 4. Mean variance explained by the single (light grey) and dual (dark grey) pRF models in the training versus validation stages (left versus right columns). Data are presented separately for voxels classified as having single (top row) versus dual (bottom row) pRFs in the partial *F*-test analysis. Error bars are *SEM*. For voxels classified as having single pRFs, there was no significant difference in variance explained by the single and dual pRF models in either the training or validation stages. For voxels classified as having dual pRFs, the dual pRF model significantly outperformed the single pRF model in both stages. This confirms that the added parameters capture additional stimulus-driven variance and are not just over-fitting noise. (* indicates statistically significant differences, $p < 0.05$).

by the extra parameters, we also performed a cross-validation analysis on all voxels in the albinism group classified as having either single (Figure 4, top row) or dual (see Figure 4, bottom row) pRFs in the partial *F*-test analysis. The "Training" column (left) in Figure 4 shows the mean %*VE* for the dual and single pRF models combined across all subjects' individual runs in the training stage. The validation column (right) displays the corresponding results averaged across all train-test combinations in the validation stage. For

single pRF voxels (see Figure 4, top row), there was no significant difference in the mean %*VE* for the single and dual pRF models in either the training or validation stages (2 tailed, independent sample *t*-tests: $p = 0.78$ and $p = 0.57$). However, for dual pRF voxels (see Figure 4, bottom row), the dual pRF model significantly outperformed the single pRF model in both the training and validation stages by comparable margins of 10.4% and 7.9%, respectively (2 tailed, independent sample *t*-tests: $p = 0.01$ and $p = 0.03$). This result confirms that the extra Gaussian parameters were not over-fitting noise but instead captured additional BOLD response features (extra peaks) that were not explained by the single pRF model. Note that the overall variance explained by both the single and dual pRF models was lower in this analysis than in those reported above for averaged data because signals from individual fMRI runs have lower signal to noise ratio (SNR; are noisier) than averaged signals. The slight reduction in variance explained by both models in the validation versus the training stage was likely caused by random differences in noise and signal quality across the individual runs.

Dual pRF symmetry and distribution across the visual field

We assessed the symmetry of dual pRFs by computing the angle formed by the two pRF centers with respect to horizontal. Again, an angle of 0 degrees indicates symmetry across the VM whereas an angle of 90° indicates symmetry across the HM. These data were sorted into 10 degree bins and histograms were made for each subject plotting the number of dual pRF voxels oriented at each angle. Figure 5 plots dual pRF angle histograms for the combined group data (top plot) and for each individual subject (bottom plots). Data for subjects with albinism are plotted in orange on the right and control subjects' data are plotted in blue on the left. The group histograms plot the mean number of dual pRF voxels oriented at each respective angle (error bars = *SEM*), whereas the individual subject histograms plot the total number of dual pRF voxels at each respective angle. As displayed in Figure 5, the albinism group's dual pRF angle data formed a clear peak centered on 0 degrees. This pattern is also observable in the data of individual subjects with albinism (3, 4, and 5). The dual pRF angle histogram of subject 1 was more sparsely populated and subject 2 showed a wider distribution of angles indicating heterogeneity in the range of angles represented in the albinism group. In contrast, the control dual pRF angle distributions showed no common central tendency. The group histograms in Figure 5 clearly show that the largest group differences and the vast majority of dual pRFs in albinism occur between bins -30 degrees
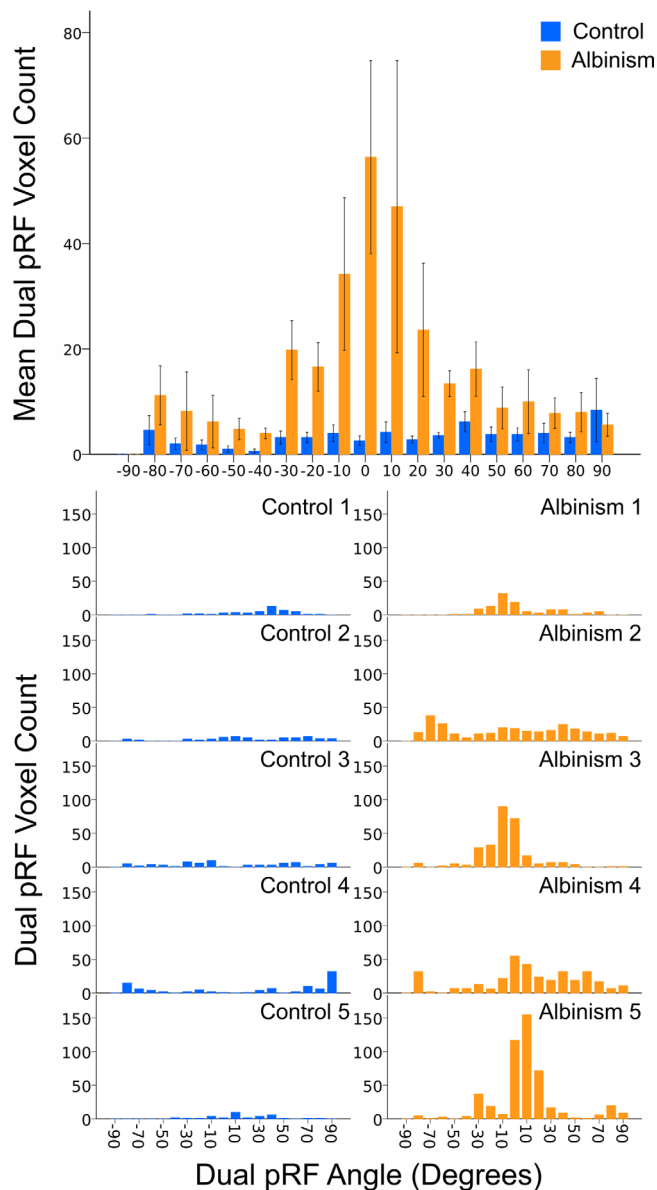
Figure 5. Histograms of dual pRF angle for groups (top) and for individual subjects (bottom). Data for subjects with albinism are plotted in orange on the right, and control subjects' data are plotted in blue on the left. The top histogram shows the group mean dual pRF voxel count versus angle formed by the dual pRF centers (degrees). Error bars are *SEM*. Lower histograms show dual pRF voxel count versus angle.

and 30 degrees with the greatest difference occurring at the 0 degree bin. Consequently, we focused all further analyses only on dual pRF voxels with angles between −30 degrees and 30 degrees.

To assess the distribution of dual pRFs across the visual field, we plotted each albinism subject's dual pRFs in the visual space in Figure 6. We limited these plots to display dual pRFs at eccentricities between 1 and 10 degrees as 95% of dual pRFs fell within that range. The circle radii represent σ for each dual pRF

Gaussian component and dual pRF pairs are connected by a thin line. Note that dual pRFs were not uniformly distributed across the visual field but were instead grouped in discrete clusters, the majority of which were in the lower visual field. The total number and extent to which dual pRFs extended outward from the VM also varied substantially across subjects.

As illustrated in Figure 2C, dual pRFs occurred less frequently on and near the VM representations whereas single pRFs occurred more frequently near the VM in albinism. To quantify this, we plot frequency histograms of dual pRF components and single pRFs versus distance from VM in Figures 7A and 7B respectively. In Figure 7A, most subjects appear to have two clear peaks on either side of a trough at the VM (x = 0). This is particularly evident in subjects 3 and 5. In contrast, single pRFs occurred most frequently close to the VM (see Figure 7B). However, reduced dual pRF frequency and increased single pRF frequency at the VM likely reflects unavoidable limitations in our ability to differentiate dual pRFs near the VM. Because dual pRF components are roughly symmetrical about the VM (see Figure 4) their responses will tend to merge near the VM and will be fit equally well by a wide single pRF model.

Dual pRF distribution relative to hemifield overlap zones in albinism

To further investigate whether the overlapping right and left hemifield representations in albinism are responsible for aberrant dual pRFs, we examined the association between dual pRF voxels and the cortical zones of right and left hemifield overlap. Note that the overlap zones were computed using the hemifield ring data while the dual pRFs were computed independently using the full field rotating wedge data. Figure 8A shows cortical surface models of subject 5's overlap map (left, repeated from Figure 1C) with the corresponding map of single versus dual pRF voxels (right, repeated from Figure 2C). Note that the large red patch of dual pRF voxels in V1 is closely associated with a green patch of hemifield overlap (see arrows). Dual pRF patches on the ventral V2 to V3 border are also closely associated with the green hemifield overlap zone in that region. However, note that single pRF zones (purple) sometimes intersect with the overlap zones indicating that some voxels in the overlap zones met our single pRF criteria. This is most notable in Figure 8A along the VM representation which forms the V1/V2v boundary.

To quantify the correspondence between the dual pRF clusters and hemifield overlap zones, we calculated the proportion of dual pRF voxels which fell in non-overlap versus overlap zones (see Figure 8B).
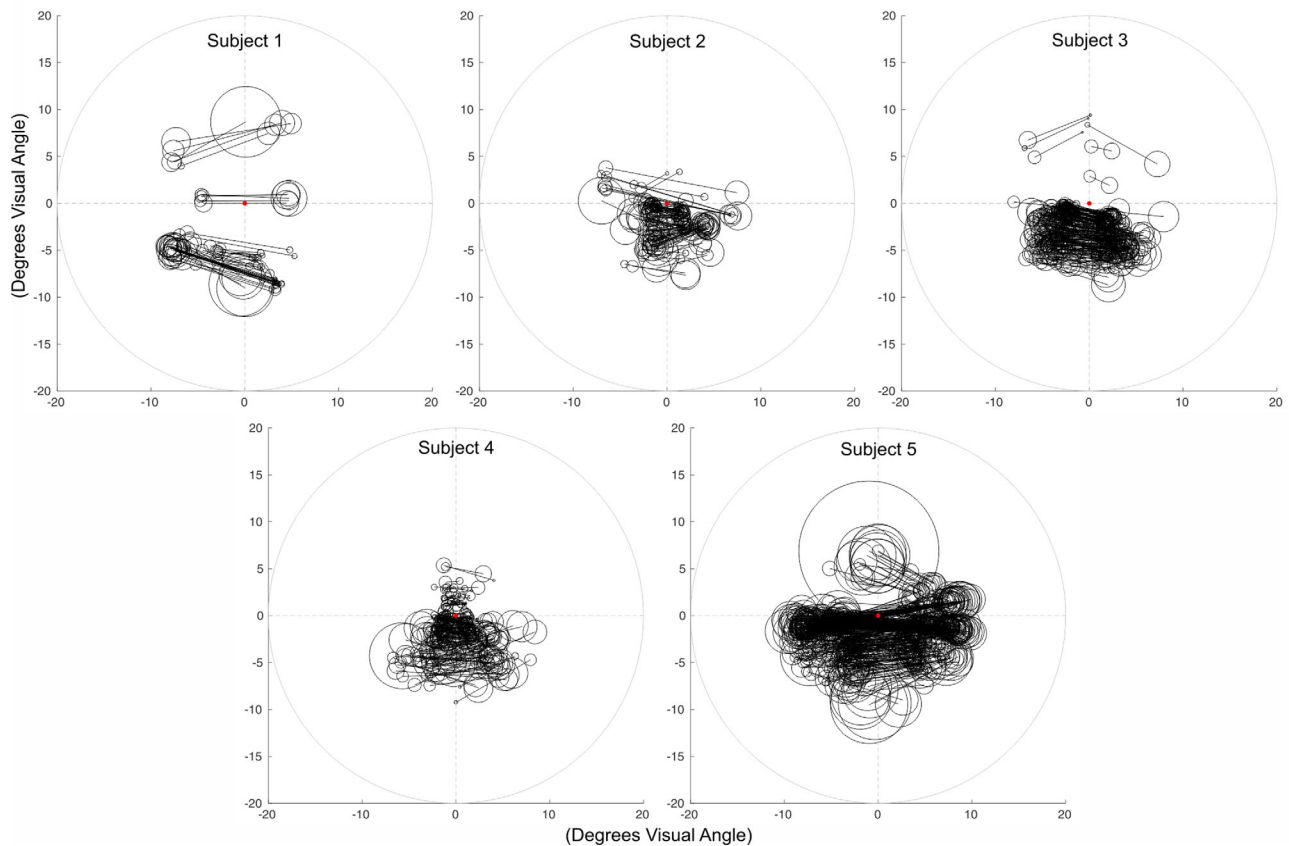
Figure 6. Visual field plots displaying dual pRFs for each subject with albinism. Circle radii represent the sigma for each dual pRF Gaussian component. Thin lines connect each dual pRF pair. Plots display all dual pRFs located between 1 and 10 degrees eccentricity with angular symmetry values (θ) between −30 and 30 degrees.

To be included in this analysis, voxels must have met the inclusion criteria for both the overlap and the pRF analysis described in Methods and have dual pRF angles between -30 degrees and 30 degrees. For the subject whose data are displayed in Figure 8A (albinism subject 5), the vast majority (approximately 86%) of dual pRF voxels fell in the overlap zones. This relationship held strongly for four of the five subjects with albinism: in subjects 1, 2, 3, and 5 the vast majority (83%–94%) of dual pRF voxels fell in the right and left hemifield overlap zones. However, in subject 4, only 52% of dual pRF voxels fell in the overlap zone. Nonetheless, for the albinism group combined, a significantly greater proportion of dual pRF voxels fell in the hemifield overlap zones than in the nonoverlap zones (80% vs. 21%, two sample, two tailed *t*-test $p = 0.0004$). This was not the case for single pRF voxels (60% vs. 40%, $p = 0.09$).

Single and dual pRF size scaling

To measure how single and dual pRF sizes scale with eccentricity, we collapsed each subject's data into 1 degree eccentricity bins and then plotted mean pRF size (σ) versus eccentricity for each bin. Data were plotted separately for V1 to V3 in albinism versus control subjects in Figure 9 (error bars = *SEM*). The first five plots in each row display individual subjects' pRF size scaling data, and the sixth plot in each row displays linear trendlines fit to the data pooled across subjects for each group. The final graphs in Figures 9A and 9B show the same data but are constrained to pRFs falling within 30 degrees polar angle of the HM. The pRFs in this zone are unaffected by the issue mentioned earlier of merged dual pRF's near the VM. This was not included in Figure 9C, as this issue only pertains to single pRF sizes. A color key in the upper left indicates color of symbols representing each visual area. Figures 9A and 9B display single pRF size scaling data for the control and albinism groups respectively, and Figure 9C displays dual pRF component size scaling for the albinism group. A three factor, univariate ANOVA (dependent variable: pRF size, factors: component laterality, visual area, and eccentricity) revealed no significant effect of component laterality (ipsi- versus contralateral) on dual pRF component size ($p = 0.08$). Therefore, we have only displayed the contralateral
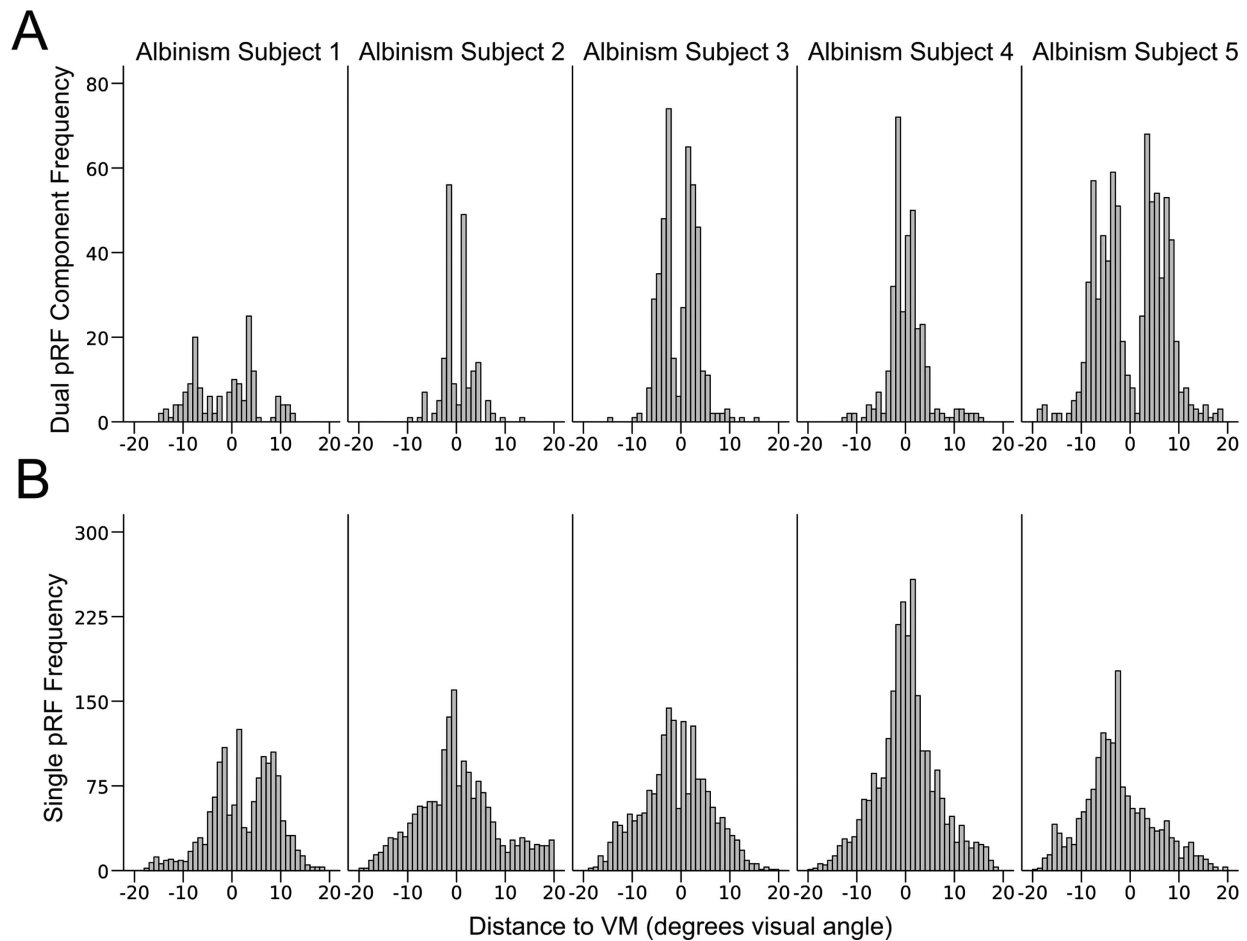
Figure 7. Frequency histograms of dual pRF components (**A**) and single pRFs (**B**) versus linear distance from VM in each subject with albinism. Note: Apparent reduced incidence of dual pRFs plus enhanced incidence of single pRFs at VM (x = 0) likely reflect inability to differentiate merged dual pRF components when close to VM.

component sizes. These analyses were also limited to eccentricities of 1 to 10 degrees for the same reasons stated above. Linear trendlines were fit for each visual area in the group data plots to portray size scaling slopes. Colored dotted lines in the group plots demark the 95% confidence interval of the group mean at each eccentricity.

Single pRF sizes were compared statistically across eccentricity, visual area, and group using a three-factor univariate ANOVA. As expected, there were highly significant main effects of both eccentricity and visual area ($p < 0.001$ for each) and a significant interaction between eccentricity and visual area ($p < 0.001$). These results reflect the consistent scaling of single pRF size with eccentricity and visual area across the control and albinism groups clearly visible in Figures 9A and 9B. Subsequent two-factor ANOVAs run on the control and albinism groups separately revealed that the main effects of eccentricity and visual area were significant for both groups individually (all p values < 0.001) but that the interaction between eccentricity and visual

area was only significant for the control group ($p < 0.001$). Post hoc Tukey HSD multiple comparison tests comparing mean single pRF size in each visual area confirmed that the mean pRF size in visual areas V1 to V3 were all significantly different from one another in both the albinism and control groups with single pRF sizes increasing with visual area.

Our initial three factor ANOVA comparing single pRF size across eccentricity, visual area, and group also revealed a significant main effect of group ($p < 0.001$) with larger single pRFs in albinism. However, we believe this group difference was influenced by the dual pRF modeling limitations near the VM in albinism noted above and illustrated in Figure 7. As dual pRFs in albinism are roughly symmetrical across the VM, the two components and their respective BOLD responses will tend to merge near the VM and be fit equally well by a large single pRF model. Indeed, we confirm in Supplementary Figure S2 that single pRF sizes and scaling are comparable for the two groups on the HM, but that single pRFs are larger in albinism on the VM.
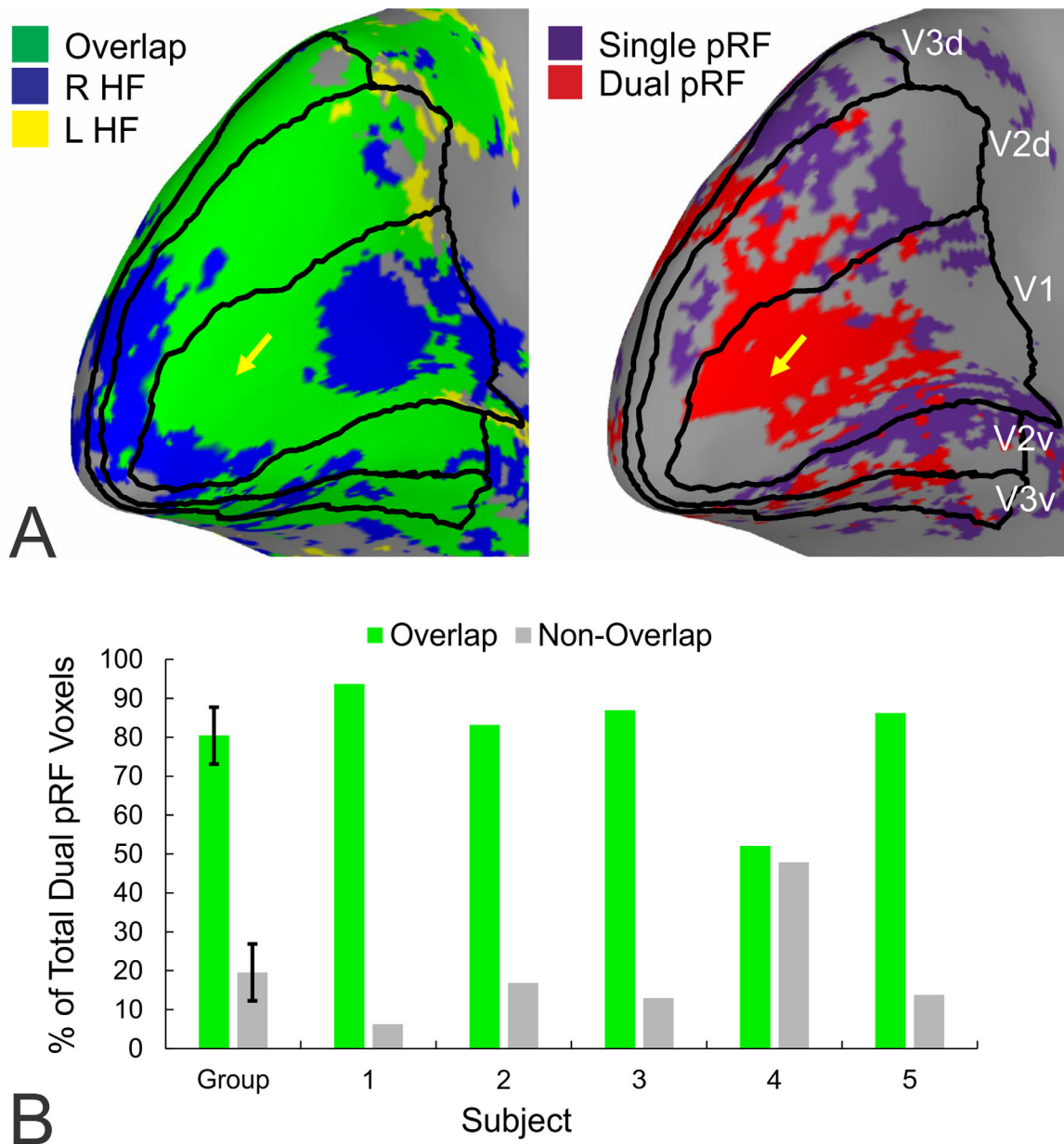
Figure 8. Dual pRF voxels often coincide with right-left hemifield overlap zones. (**A**) Repeat of Figures 1C and 2C. Note close correspondence of red dual pRF cluster (right arrow) with large green overlap zone (left arrow). (**B**) Proportion of total dual pRF voxels falling in overlap versus non-overlap zones for all five subjects with albinism. Error bars are *SEM*.

Enhancement of single pRF size on the VM in albinism was also clearly exacerbated by increasing eccentricity and visual area where dual pRF components are larger and more likely to merge. To correct for this, we plot single pRF size scaling exclusively for pRFs falling within 30 degrees polar angle of the HM in the rightmost plots of Figures 9A and 9B as these voxels are not affected by this issue. This constraint has little effect on control's single pRF slopes in Figure 9A, but reduces the size scaling slopes for the albinism group in Figure 9B.

Finally, we compared dual pRF component sizes to single pRF sizes in the albinism group across eccentricity and visual area in a univariate three factor ANOVA (dependent variable: pRF size; factors: type [single/dual], eccentricity, and visual area). This test again showed significant eccentricity and visual area effects ($p < 0.001$ for each), but also revealed a significant effect of pRF type ($p < 0.001$) and significant interactions of eccentricity*visual area, eccentricity*type, and visual area*type ($p = 0.028$, $p < 0.001$, and $p < 0.001$, respectively). These effects
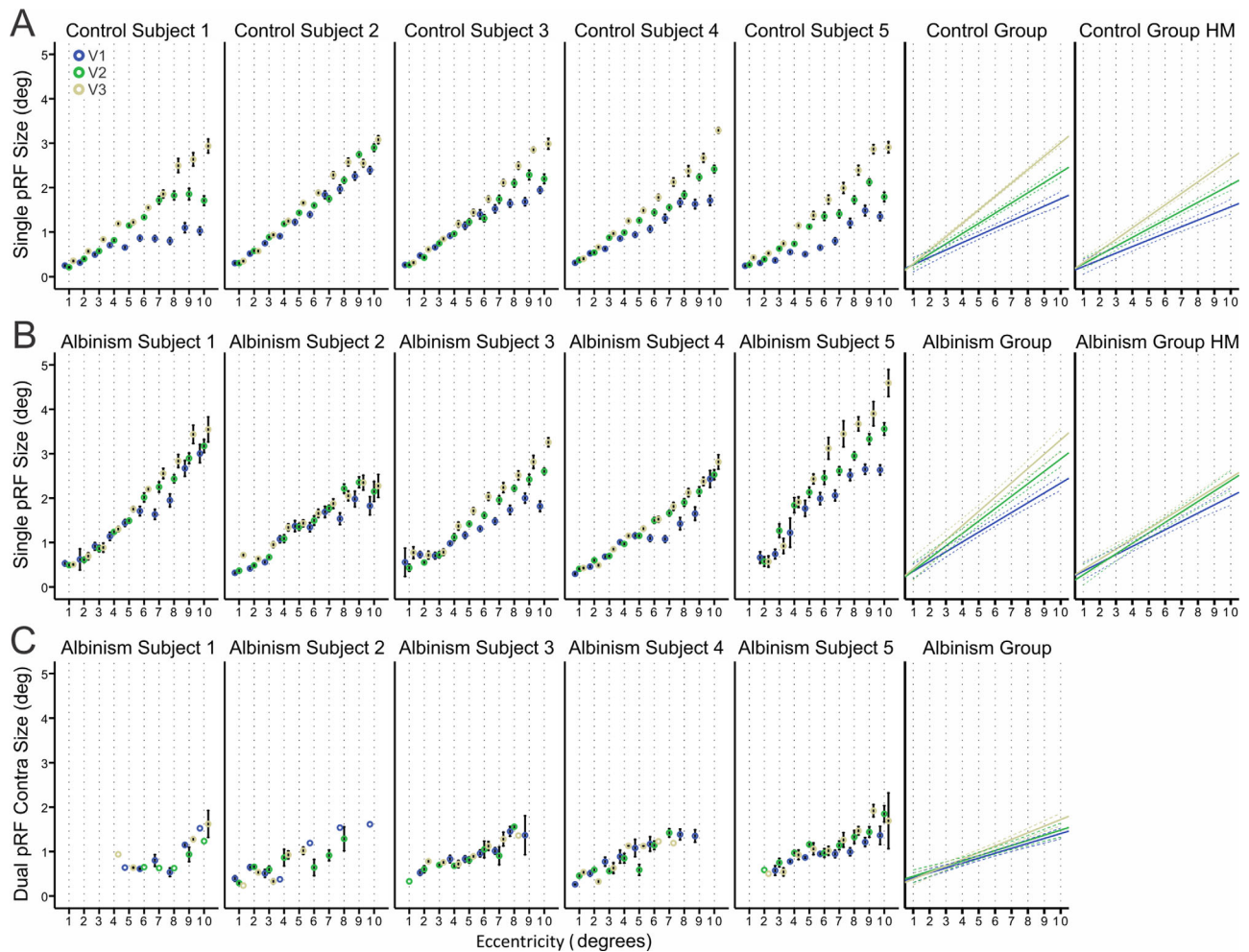
Figure 9. pRF size versus eccentricity for V1 to V3 in albinism and controls. A visual area color code is displayed in the upper left. The first five plots in each row display individual subjects' pRF size data. The sixth plot in each row shows linear trend lines fit to the data pooled across subjects. The final plots in rows A and B display data for only single pRFs falling within 30 degrees polar angle of the HM. Solid lines are linear trend lines fit for each visual area. Colored dotted lines demark the 95% confidence interval of the group mean. (**A**) Single pRFs in control subjects. (**B**) Single pRFs in subjects with albinism. (**C**) Contralateral dual pRF component in subjects with albinism. There was no difference in size for contra- versus ipsilateral dual pRF components. Error bars in individual subject plots are *SEM*.

are evident when visually comparing the dual pRF component scaling data to the single pRFs in Figure 9 as the dual components are consistently smaller than their single pRF counterparts and also scale less steeply with eccentricity and visual area. The "merging" issue at the VM discussed earlier likely contributed to this result; however, dual pRF component size scaling is still clearly reduced even when compared to single pRFs restricted to the HM (Figure 9B far right versus 9C far right). Although the ipsi- and contralateral dual pRF component sizes differed for some individual voxels, as mentioned previously, a subsequent ANOVA comparing the size of contralateral and ipsilateral dual pRF components across eccentricity showed no significant effect of component laterality ($p = 0.08$). However, there were, significant main effects of

eccentricity ($p < 0.001$), visual area ($p = 0.027$), and an interaction between eccentricity and laterality ($p = 0.002$). Nonetheless, our post hoc Tukey test comparing dual pRF component sizes of each visual area failed to show significant differences in dual pRF component size between any pair of visual areas. This is consistent with the reduced dual pRF size scaling across visual areas evident in Figure 9C.

Correlation of dual pRF voxel incidence and fixation stability

There was also a significant relationship between dual pRF incidence and fixation stability. We correlated
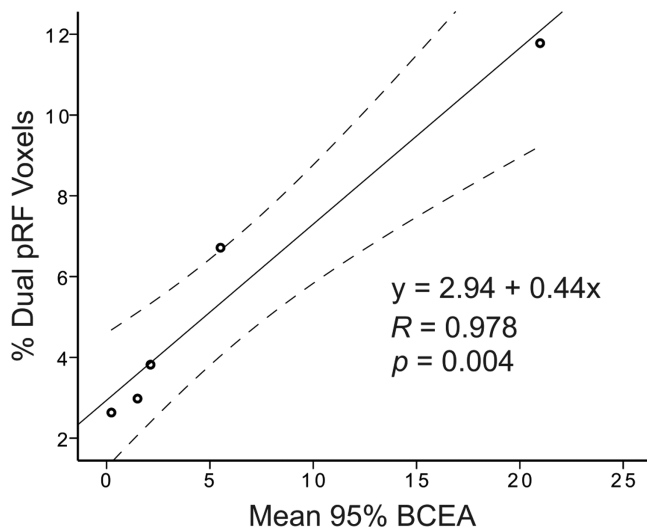
Figure 10. Scatter plot of percent dual pRF incidence versus mean OPKO 95% BCEA fixation stability for the right eye and left eyes in subjects with albinism. The equation describes the linear regression fit (solid line). Dotted lines represent the 95% confidence interval. *R* is Pearson's correlation, and *p* indicates the correlation significance.

dual pRF voxel incidence with subjects' mean 95% BCEA values for the right and left eye measured in our OPKO fixation stability procedure (Figure 10). Again, this analysis was run only on dual pRF voxels whose dual pRF symmetry angles (θ) fell between -30 degrees and 30 degrees. Percent dual pRF voxel incidence correlated significantly with subjects' mean 95% BCEA measurements ($R = 0.978$, $p = 0.004$).

Discussion

In this study, we examined the functional organization of visual cortex in subjects with albinism. In particular, we focused on the effects of aberrant retinotopy on characteristics of single voxel pRFs. In all subjects with albinism, we observed partial representations of the ipsilateral visual hemifield that were superimposed on the normal contralateral hemifield representation within each hemisphere (see Supplementary Figure S1), consistent with previous reports (Hoffmann et al., 2003; Kaule et al., 2014; Morland et al., 2001; von dem Hagen, Houston, Hoffmann, & Morland, 2007). We predicted that such overlaid representations would result in single voxels having bilateral dual pRFs. As predicted, we successfully modeled numerous unequivocal cases of dual pRFs in three of our five subjects with albinism (subjects 3, 4, and 5). We also observed many dual pRFs in the other two subjects albeit in smaller, more diffuse

clusters. Dual pRF voxels occurred preferentially in cortical zones of the right and left hemifield overlap. However, despite the consistent association between dual pRF voxels and the hemifield overlap zones, not all voxels in the overlap zones had clearly discernible dual pRFs, and many displayed responses indistinguishable from a single pRF. We present evidence suggesting these apparent single pRFs in the overlap zones likely reflect the effect of unavoidable dual pRF merging near the VM in albinism. These findings provide clarity in light of recent conflicting reports of whether dual pRF voxels exist in albinism (Ahmadi et al., 2019; Alvarez et al., 2020; Carvalho et al., 2020). To our knowledge, this is the first study to distinguish between dual and single pRF voxels within individual subjects with albinism and report the size scaling of ipsi- and contralateral dual pRF model components. In contrast to recent attempts, which modeled dual pRFs in albinism explicitly as mirror-symmetrical Gaussian fields, our model optimized the two pRFs independently allowing the two fields to be placed at any pair of angular positions. Even so, our analysis indicated that the two pRF components tend to be positioned approximately (although not always precisely) at mirror image locations across the VM (see Figure 5). Our approach of independently optimizing each pRF component was vital to successfully model these not quite symmetrical dual pRFs. This approach also allowed us to independently measure size scaling of the contra- and ipsilateral dual pRF components with eccentricity and visual area. It is also notable that dual pRFs were not uniformly distributed across the visual field (see Figure 6). Consequently, tailoring future psychophysical experiments to each albinism subject's unique dual pRF map may prove useful in detecting potential perceptual consequences of retinocortical miswiring.

Aberrant retinotopic organization in albinism

We observed substantially overlapping right and left hemifield representations in each cortical hemisphere of all subjects with albinism. This pattern is consistent with the retinal line of decussation (which is normally centered on the VM) being shifted temporally with the misrouted temporal afferents reaching the same locations in ipsilateral visual cortex as their mirrored nasal counterparts. It is worth noting that the albinism subtypes represented in our cohort included OA, OCA1B, and OCA2, indicating that such aberrant representations are not unique to any one albinism subtype. The mean percentage of cortex responding to both right and left hemifield stimuli (overlap zones) varied significantly across subjects (see Figure 1: 39.2%–69.7%) as did the line of decussation shift (see Table 3: 3.0–13.8 degrees). This is consistent with the

known variability in extent of miswiring at the optic chiasm across the albinism population as a whole (Creel, Spekreijse, & Reits, 1981; Hoffmann, Lorenz, Morland, & Schmidtborn, 2005; Hoffmann et al., 2003; Kaule et al., 2014; von dem Hagen et al., 2007). The extent of overlap was relatively constant across V1 to V3 within individuals (see Figure 1), which agrees with previous studies showing that the aberrant ipsilateral representation set up by the retinocortical afferents to V1 is propagated to subsequent stages of the visual hierarchy (Kaule et al., 2014; Wolynski, Kanowski, Meltendorf, Behrens-Baumann, & Hoffmann, 2010).

Subjects with albinism have voxels with single and dual pRFs

Our analysis suggests that the partial superposition of opposite hemifield representations in albinism produces voxels having either single or dual pRFs. This was qualitatively evident in the rotating wedge time course data as some voxels responded with ten robust peaks (twice per period), whereas other voxels responded with the expected five peaks (once per period; see Figure 2A). Quantitative modeling indicated that these double responses are best predicted by a dual pRF model, and cross-validation confirmed that the additional pRF parameters retain their added predictive value across separate training and test datasets. Voxels meeting our conservative dual pRF criteria were numerous in subjects with albinism (4%–15%) but not controls (1%–3%). Moreover, a close examination of the pRF fits of such voxels in controls showed that these cases were not convincing, but were instead instances of over-fitting and infrequent partial-voluming across the midline. The comparable incidence of dual pRF voxels across V1 to V3 in albinism again supports the idea that the aberrant ipsilateral field representation set up by peripheral miswiring is propagated up the visual hierarchy.

Dual pRF symmetry

Dual pRF symmetry angles in our albinism group peaked at 0 degrees indicating that the two fields tended to be symmetric across the VM (see Figure 5). These results affirm previous literature that suggests opposite hemifield representations in albinism are superimposed in a mirror symmetrical manner (Hoffmann et al., 2003). However, it is worth noting that some individual dual pRFs are "tilted" by as much as 30 degrees relative to horizontal suggesting that the overlap of the opposite hemifield representations may not always be in perfect retinotopic register, at least within localized regions.

This was also noted in (Woertz et al., 2020) where there were sometimes significant mismatches in eccentricity mapping over restricted cortical zones. Consequently, in order to best fit all dual pRF responses in albinism, models should not be rigidly symmetrical, but instead incorporate some flexibility as described here or by using the recently developed "micro-probing" technique described by (Carvalho et al., 2020). On the other hand, the few "dual pRFs" that were observed in controls showed no clear bias toward any angular orientation. This further supports our interpretation that dual pRFs observed in controls likely arise for artifactual reasons such as model over-fitting.

Distribution of dual pRF voxels relative to hemifield overlap zones

Given the partial superposition of opposite hemifield representations within visual cortex in albinism, one might expect that all voxels within these overlap zones would have clear dual pRFs, whereas all voxels outside these zones would all have clear single pRFs. This was not the case. Importantly, the vast majority of dual pRF voxels in albinism were located, as expected, in regions of right-left hemifield overlap (see Figure 8). This suggests that the cortical superposition of opposite hemifields in albinism results in voxels with dual pRFs. However, numerous voxels within the overlap zones in all subjects met our conservative single pRF criteria. We show that this is likely due to unavoidable dual pRF modeling limitations near the VM in albinism. It is important to note that the successful modeling of dual pRFs could only occur when there was sufficient separation between the two peaks of each dual response (5 dual peak pairs); otherwise, the dual pRF model would perform no better than a "wide" single pRF model. As dual pRFs in albinism are roughly symmetrical across the VM (see Figure 5), the two pRF component responses will merge near the VM and be fit equally well by large single pRFs. This is consistent with our observations of reduced dual pRF frequency on the VM (see Figure 7A), enhanced single pRF frequency on the VM (see Figure 7B), and large apparent single pRFs on the VM in albinism (Supplementary Figure S2), and likely explains why many apparent single pRF voxels occur in the overlap zones. Moreover, lack of separation between the dual pRF BOLD responses near the VM suggests that our reported incidence of dual pRFs is likely an under- rather than over-estimate. Finally, the acquisition of the overlap maps and dual pRF modeling data using two different mapping paradigms (monocular hemifield expanding rings versus full field binocular rotating wedge) may have contributed to the lack of perfect correspondence between the distribution of dual pRFs and the hemifield overlap zones.

pRF size

Single pRFs sizes in albinism scaled with eccentricity and visual area in a manner that was qualitatively similar to controls (see Figures 9A, 9B). When compared statistically, we found that single pRFs were larger overall in the albinism group. However, as explained above, we believe this difference is likely a consequence of the symmetrical dual pRF components' responses merging near the VM and being fit well by wide single pRF models. When constrained to the HM, single pRF size scaling between groups was much more comparable (see Figures 9A, 9B, Supplementary Figure S2). Differences in stimulus width between the two groups may have also contributed to the group difference; however, as single pRF sizes were very similar on the HM, we do not think this was a primary cause. Dual pRF components in albinism also clearly scaled with eccentricity, but were slightly smaller overall, and visual area scaling was less clear. Reduced dual pRF component sizes and scaling may also be a consequence of the merging issue described above as larger dual pRF components in higher visual areas would be more prone to merge and be misclassified as wide single pRFs. This explanation is indirectly supported in Supplementary Figure S2 where single pRFs size enhancement on the VM in albinism is clearly exacerbated by both eccentricity and visual area. Nonetheless, dual pRF component size scaling was still clearly shallower even when compared to single pRFs restricted to the HM in albinism (see Figure 9). Finally, we observed differences in the ipsi- and contralateral component sizes in some individual dual pRFs; however, there was no significant difference between the dual component sizes suggesting that, overall, the two components scale similarly.

Limitations, potential artifacts, and caveats

The presence of dual pRFs in albinism was expected given the previously known superposition of opposite hemifield representations in visual cortex. Nevertheless, one must consider potential artifactual causes. One potential cause might be that individual imaging voxels encompass retinotopically disparate locations across sulci or across the midline. Although it is possible that some optimally situated voxels might show such effects, the dual pRF voxels we observed in albinism often occurred in large clusters far from the midline and were typically positioned entirely within gray matter. Furthermore, if the dual pRFs we observed were solely an artifact of such partial-voluming, then we would have expected to observe comparable numbers of dual pRFs in our control subjects. This was not the case.

One might also wonder if dual pRFs somehow result from fixational instability or nystagmus. Indeed, our OPKO 95% BCEA measure of fixational stability was positively correlated with the incidence of dual pRFs (see Figure 10). However, it is extremely difficult to imagine how random instability or even nystagmus could artifactually create a population of dual pRF voxels with components that are mirror symmetric and at a variety of positions relative to the VM. Furthermore, a recent study (Ahmadi et al., 2019) showed that "fixation jittering" mimicking nystagmus in controls fails to produce comparable effects in controls. Previous retinotopic mapping studies in other populations with nystagmus have also shown that moderate nystagmus (50% BCEA of 1–3 degrees) has little or no effect on the fMRI response (Baseler, Brewer, Sharpe, Morland, Jägle, & Wandell, 2002). All but one of our subjects' BCEAs fell within this range. A more likely explanation for the correlation of BCEA and dual pRF incidence is that both reflect aberrant central visual system organization and, consequently, both tend to increase with the severity of the albinism syndrome.

The slight differences in stimuli used in the albinism and control datasets available for this study are a limitation, and stimulus width discrepancies confound our ability to make conclusive pRF size comparisons between groups. However, as single pRF sizes were comparable on the HM between groups we do not think that this confound played a large role. In addition, slight differences in wedge width and timing could not explain the existence of dual responses in albinism.

The dual pRF modeling limitations near the VM described above are also a limitation of this study, and likely any fMRI study attempting to model dual pRFs in albinism. As dual pRFs in albinism are roughly symmetrical about the VM, their BOLD response peaks will inevitably merge near the VM to form a single response fit equally well by a large single pRF. Moreover, as retino-cortical miswiring in albinism involves an aberrant temporal shift in the line of decussation, which is typically defined by the VM, in milder cases with small shifts, nearly all the dual pRFs will be in close proximity to the VM making them difficult to distinguish from single pRFs. This could explain conflicting reports and the variable success of dual pRF models in the recent albinism literature (Ahmadi et al., 2019; Alvarez et al., 2020).

Finally, albinism is a relatively rare condition, and it is even more uncommon to find people with albinism and fixation stable enough for retinotopic mapping. Consequently, obtaining large numbers of suitable subjects is problematic and is a potential limitation of this study. However, we feel that the results reported here are of sufficient interest to warrant future studies that seek to corroborate these findings in a larger subject cohort.

Albinism is heterogeneous both peripherally and centrally

Finally, there is a great deal of genetic heterogeneity within the albinism population. Different mutations in the melanin synthesis pathway give rise to different subtypes of albinism as well as heterogeneity in retinal morphology (Kruijt, de Wit, Bergen, Florijn, Schalij-Delfos, & van Genderen, 2018; Lee, Woertz, Visotcky, Wilk, Heitkotter, Linderman, Tarima, Summers, Brooks, Brilliant, Antony, Lujan, & Carroll, 2018; Montoliu et al., 2014; Oetting & King, 1999; Patel, Hayward, Tailor, Nyanhete, Ahlfors, Gabriel, Jannini, Abbou-Rayyah, Henderson, Nischal, Islam, Bitner-Glindzicz, Hurst, Valdivia, Zanolli, Moosajee, Brookes, Papadopoulos, Khaw, Cullup, Jenkins, Dahlmann-Noor, & Sowden, 2019; Prieur & Rebsam, 2017; Simeonov et al., 2013; Wilk et al., 2014). However, specific genetic details for individual patients have not been included in the vast majority of previous imaging studies of albinism. In this study, we intentionally selected subjects with albinism to represent a diverse sampling of albinism subtypes (see Table 1) in order to enhance the probability of observing variation in the central organization of visual pathways. Interestingly we saw disrupted central organization even in subjects with the recently described "tri-allelic" form of albinism (Grønskov, Jespersgaard, Bruun, Harris, Brondum-Nielsen, Andresen, & Rosenberg, 2019; Monferme, Lasseaux, Duncombe-Poulet, Hamel, Defoort-Dhellemmes, Drumare, Zanlonghi, Dollfus, Perdomo, Bonneau, Korobelnik, Plaisant, Michaud, Pennamen, Rooryck-Thambo, Morice-Picard, Paya, & Arveiler, 2019; Norman, O'Gorman, Gibson, Pengelly, Baralle, Ratnayaka, Griffiths, Rose-Zerilli, Ranger, Bunyan, Lee, Page, Newall, Shawkat, Mattocks, Ward, Ennis, & Self, 2017). Although our sample is not nearly large enough to draw strong correlations among genetic, retinal, and central factors, we did observe variation across our albinism sample in the extent of hemifield overlap, pRF size, incidence of dual pRFs, and the distribution of dual pRFs across the visual field. We speculate that genetic factors responsible for the range of subtypes in albinism may also underlie the variations in retinocortical organization observed in our dual pRF analysis. If so, this suggests that in a larger sample of subjects with albinism, this approach will prove productive for linking genetic and morphological factors with unique patterns of central miswiring not only in albinism but in a variety of inherited vision disorders (Hoffmann & Dumoulin, 2015). Accounting for individual variability in factors such as dual pRF location and topography in albinism may also allow us to better target future tests for potential perceptual effects of retinocortical miswiring, and ultimately aid in our understanding of the perceptual relevance of retinotopic organization within the visual system.

Conclusions

This study shows that retinocortical miswiring in albinism results in single imaging voxels with bilateral dual pRFs. Voxels with dual pRFs are numerous in subjects with albinism but not control subjects and occur selectively in cortical regions where the right and left hemifield representations are superimposed. Our results agree with previous studies which predict that dual pRFs in albinism are positioned at approximately mirror image locations across the VM but suggest that this symmetry is not always precise. Thus, in order to accurately fit responses from all dual pRF voxels, models cannot be rigidly mirror symmetrical, but must instead incorporate some flexibility. Finally, dual pRFs in albinism were not evenly distributed across the visual field, but were instead uniquely clustered within a portion of the visual field for each subject. In the future, mapping subjects' unique dual pRF distributions could guide spatially focused psychophysical tests aimed at revealing previously undetected perceptual consequences of retinocortical miswiring in albinism.

Keywords: albinism, population receptive field (pRF) modeling, retinotopic mapping, human

References

Ahmadi, K., Fracasso, A., van Dijk, J. A., Kruijt, C., van Genderen, M., Dumoulin, S. O., . . . Hoffmann, M. B. (2019). Altered organization of the visual cortex in FHONDA syndrome. *Neuroimage, 190*, 224–231.

Ahmadi, K., Herbik, A., Wagner, M., Kanowski, M., Thieme, H., & Hoffmann, M. B. (2019). Population receptive field and connectivity properties of the early visual cortex in human albinism. *Neuroimage, 202*, 116105.

Alvarez, I., Smittenaar, R., Handley, S. E., Liasis, A., Sereno, M. I., Schwarzkopf, D. S., . . . Clark, C. A. (2020). Altered visual population receptive fields in human albinism. *Cortex, 128*, 107–123.

Amano, K., Wandell, B. A., & Dumoulin, S. O. (2009). Visual field maps, population receptive field sizes, and visual field coverage in the human MT+ complex. *Journal of Neurophysiology, 102*(5), 2704–2718.

Arcaro, M. J., McMains, S. A., Singer, B. D., & Kastner, S. (2009). Retinotopic organization of human ventral visual cortex. *Journal of Neuroscience, 29*(34), 10638–10652.

Bandettini, P. A., Jesmanowicz, A., Wong, E. C., & Hyde, J. S. (1993). Processing strategies for time-course data sets in functional MRI of the human brain. *Magnetic Resonance in Medicine, 30*(2), 161–173.

Baseler, H. A., Brewer, A. A., Sharpe, L. T., Morland, A. B., Jägle, H., & Wandell, B. A. (2002). Reorganization of human cortical maps caused by inherited photoreceptor abnormalities. *Nature Neuroscience, 5*(4), 364–370.

Carvalho, J., Invernizzi, A., Ahmadi, K., Hoffmann, M. B., Renken, R. J., & Cornelissen, F. W. (2020). Micro-probing enables fine-grained mapping of neuronal populations using fMRI. *Neuroimage, 209*, 116423.

Cox, R. W. (1996). AFNI: software for analysis and visualization of functional magnetic resonance neuroimages. *Computers and Biomedical Research, 29*(3), 162–173.

Creel, D., Spekreijse, H., & Reits, D. (1981). Evoked potentials in albinos: efficacy of pattern stimuli in detecting misrouted optic fibers. *Electroencephalography and Clinical Neurophysiology, 52*(6), 595–603.

Datta, R., & DeYoe, E. A. (2009). I know where you are secretly attending! The topography of human visual attention revealed with fMRI. *Vision Research, 49*(10), 1037–1044.

DeYoe, E. A., Carman, G. J., Bandettini, P., Glickman, S., Wieser, J., Cox, R., . . . Miller, D. et al. (1996). Mapping striate and extrastriate visual areas in human cerebral cortex. *Proceedings of the National Academy of Sciences of the United States of America, 93*(6), 2382–2386.

Dumoulin, S. O., & Wandell, B. A. (2008). Population receptive field estimates in human visual cortex. *Neuroimage, 39*(2), 647–660.

Engel, S. A., Glover, G. H., & Wandell, B. A. (1997). Retinotopic organization in human visual cortex and the spatial precision of functional MRI. *Cerebral Cortex, 7*(2), 181–192.

Fujii, G. Y., De Juan, E., Jr., Humayun, M. S., Sunness, J. S., Chang, T. S., & Rossi, J. V. (2003). Characteristics of visual loss by scanning laser ophthalmoscope microperimetry in eyes with subfoveal choroidal neovascularization secondary to age-related macular degeneration. *American Journal of Ophthalmology, 136*(6), 1067–1078.

Grønskov, K., Jespersgaard, C., Bruun, G. H., Harris, P., Brondum-Nielsen, K., Andresen, B. S., . . . Rosenberg, T. (2019). A pathogenic haplotype, common in Europeans, causes autosomal recessive albinism and uncovers missing heritability in OCA1. *Scientific Reports, 9*(1), 645.

Guillery, R. W., Hickey, T. L., Kaas, J. H., Felleman, D. J., Debruyn, E. J., & Sparks, D. L. (1984). Abnormal central visual pathways in the brain of an albino green monkey (Cercopithecus aethiops). *Journal of Comparative Neurology, 226*(2), 165–183.

Hansen, K. A., Kay, K. N., & Gallant, J. L. (2007). Topographic organization in and near human visual area V4. *Journal of Neuroscience, 27*(44), 11896–11911.

Hoffmann, M. B., & Dumoulin, S. O. (2015). Congenital visual pathway abnormalities: a window onto cortical stability and plasticity. *Trends in Neurosciences, 38*(1), 55–65.

Hoffmann, M. B., Kaule, F. R., Levin, N., Masuda, Y., Kumar, A., & Gottlob, I. et al. (2012). Plasticity and stability of the visual system in human achiasma. *Neuron, 75*(3), 393–401.

Hoffmann, M. B., Lorenz, B., Morland, A. B., & Schmidtborn, L. C. (2005). Misrouting of the optic nerves in albinism: estimation of the extent with visual evoked potentials. *Investigative Ophthalmology and Visual Science, 46*(10), 3892–3898.

Hoffmann, M. B., Tolhurst, D. J., Moore, A. T., & Morland, A. B. (2003). Organization of the visual cortex in human albinism. *Journal of Neuroscience, 23*(26), 8921–8930.

Horton, J. C., & Hoyt, W. F. (1991). The representation of the visual field in human striate cortex. A revision of the classic Holmes map. *Archives of Ophthalmology, 109*(6), 816–824.

Kaule, F. R., Wolynski, B., Gottlob, I., Stadler, J., Speck, O., & Kanowski, M. et al. (2014). Impact of chiasma opticum malformations on the organization of the human ventral visual cortex. *Human Brain Mapping, 35*(10), 5093–5105.

Kruijt, C. C., de Wit, G. C., Bergen, A. A., Florijn, R. J., Schalij-Delfos, N. E., & van Genderen, M. M. (2018). The phenotypic spectrum of albinism. *Ophthalmology, 125*(12), 1953–1960.

Lee, D. J., Woertz, E. N., Visotcky, A., Wilk, M. A., Heitkotter, H., & Linderman, R. E. et al. (2018). The Henle fiber layer in albinism: comparison to normal and relationship to outer nuclear layer thickness and foveal cone density. *Investigative Ophthalmology and Visual Science, 59*(13), 5336–5348.

Monferme, S., Lasseaux, E., Duncombe-Poulet, C., Hamel, C., Defoort-Dhellemmes, S., & Drumare, I. et al. (2019). Mild form of oculocutaneous albinism type 1: phenotypic analysis of compound heterozygous patients with the R402Q variant of the TYR gene. *British Journal of Ophthalmology, 103*(9), 1239–1247.

Montoliu, L., Grønskov, K., Wei, A. H., Martinez-Garcia, M., Fernandez, A., & Arveiler, B. et al. (2014). Increasing the complexity: new genes and new types of albinism. *Pigment Cell Melanoma Research, 27*(1), 11–18.

Morland, A. B., Baseler, H. A., Hoffmann, M. B., Sharpe, L. T., & Wandell, B. A. (2001). Abnormal retinotopic representations in human visual cortex revealed by fMRI. *Acta Psychologica, 107*(1-3), 229–247.

Norman, C. S., O'Gorman, L., Gibson, J., Pengelly, R. J., Baralle, D., & Ratnayaka, J. A. et al. (2017). Identification of a functionally significant tri-allelic genotype in the Tyrosinase gene (TYR) causing hypomorphic oculocutaneous albinism (OCA1B). *Scientific Reports, 7*(1), 4415.

Oetting, W. S., & King, R. A. (1999). Molecular basis of albinism: mutations and polymorphisms of pigmentation genes associated with albinism. *Human Mutation, 13*(2), 99–115.

Oetting, W. S., Summers, C. G., & King, R. A. (1994). Albinism and the associated ocular defects. *Metab Pediatr Syst Ophthalmol, 17*(1-4), 5–9.

Olman, C. A., Bao, P., Engel, S. A., Grant, A. N., Purington, C., & Qiu, C. et al. (2018). Hemifield columns co-opt ocular dominance column structure in human achiasma. *Neuroimage, 164*, 59–66.

Patel, A., Hayward, J. D., Tailor, V., Nyanhete, R., Ahlfors, H., & Gabriel, C. et al. (2019). The Oculome Panel Test: next-generation sequencing to diagnose a diverse range of genetic developmental eye disorders. *Ophthalmology, 126*(6), 888–907.

Pitzalis, S., Galletti, C., Huang, R. S., Patria, F., Committeri, G., & Galati, G. et al. (2006). Wide-field retinotopy defines human cortical visual area v6. *Journal of Neuroscience, 26*(30), 7962–7973.

Pitzalis, S., Sereno, M. I., Committeri, G., Fattori, P., Galati, G., Patria, F., . . . Galletti, C. (2010). Human v6: the medial motion area. *Cerebral Cortex, 20*(2), 411–424.

Prieur, D. S., & Rebsam, A. (2017). Retinal axon guidance at the midline: Chiasmatic misrouting and consequences. *Developmental Neurobiology, 77*(7), 844–860.

Puckett, A. M., & DeYoe, E. A. (2015). The attentional field revealed by single-voxel modeling of fMRI time courses. *Journal of Neuroscience, 35*(12), 5030–5042.

Raz, J., Zheng, H., Ombao, H., & Turetsky, B. (2003). Statistical tests for fMRI based on experimental randomization. [Research Support, U S Gov't, Non-P H S Research Support, U S Gov't, P H S]. *Neuroimage, 19*(2 Pt 1), 226–232.

Saad, Z. S., DeYoe, E. A., & Ropella, K. M. (2003). Estimation of FMRI response delays. *Neuroimage, 18*(2), 494–504.

Sereno, M. I., Dale, A. M., Reppas, J. B., Kwong, K. K., Belliveau, J. W., & Brady, T. J., et al. (1995). Borders of multiple visual areas in humans revealed by functional MRI. *Science, 268*(268), 889–893.

Sereno, M. I., Pitzalis, S., & Martinez, A. (2001). Mapping of contralateral space in retinotopic coordinates by a parietal cortical area in humans. *Science, 294*(5545), 1350–1354.

Silver, M. A., & Kastner, S. (2009). Topographic maps in human frontal and parietal cortex. *Trends in Cognitive Science, 13*(11), 488–495.

Simeonov, D. R., Wang, X., Wang, C., Sergeev, Y., Dolinska, M., & Bower, M. et al. (2013). DNA variations in oculocutaneous albinism: an updated mutation list and current outstanding issues in molecular diagnostics. *Human Mutation, 34*(6), 827–835.

Swisher, J. D., Halko, M. A., Merabet, L. B., McMains, S. A., & Somers, D. C. (2007). Visual topography of human intraparietal sulcus. *Journal of Neuroscience, 27*(20), 5326–5337.

Tootell, R. B., Mendola, J. D., Hadjikhani, N. K., Liu, A. K., & Dale, A. M. (1998). The representation of the ipsilateral visual field in human cerebral cortex.

Proceedings of the National Academy of Sciences of the United States of America, 95(3), 818–824.

von dem Hagen, E. A., Houston, G. C., Hoffmann, M. B., & Morland, A. B. (2007). Pigmentation predicts the shift in the line of decussation in humans with albinism. *European Journal of Neuroscience, 25*(2), 503–511.

Wandell, B. A., Dumoulin, S. O., & Brewer, A. A. (2007). Visual field maps in human cortex. *Neuron, 56*(2), 366–383.

Wandell, B. A., & Winawer, J. (2011). Imaging retinotopic maps in the human brain. *Vision Research, 51*(7), 718–737.

Wilk, M. A., McAllister, J. T., Cooper, R. F., Dubis, A. M., Patitucci, T. N., & Summerfelt, P. et al. (2014). Relationship between foveal cone specialization and pit morphology in albinism.

Investigative Ophthalmology and Visual Science, 55(7), 4186–4198.

Wilk, M. A., Wilk, B. M., Langlo, C. S., Cooper, R. F., & Carroll, J. (2017). Evaluating outer segment length as a surrogate measure of peak foveal cone density. *Vision Research, 130*, 57–66.

Woertz, E. N., Wilk, M. A., Duwell, E., Mathis, J., Carroll, J., & DeYoe, E. A. (2020). The relationship between cone density in the retina and cortical magnification in human albinism. *Journal of Vision, 20*(6), 10.

Wolynski, B., Kanowski, M., Meltendorf, S., Behrens-Baumann, W., & Hoffmann, M. B. (2010). Self-organisation in the human visual system–visuo-motor processing with congenitally abnormal V1 input. *Neuropsychologia, 48*(13), 3834–3845.